Geochimica et Cosmochimica Acta
June 2018, Volume 230, Pages 137-154
http://dx.doi.org/10.1016/j.gca.2018.03.026
http://archimer.ifremer.fr/doc/00436/54712/

Nickel distribution and isotopic fractionation in a Brazilian lateritic regolith: coupling Ni isotopes and Ni K-edge XANES.

Ratié G. [1, 2, 3, *], Garnier J. [2], Calmels D. [1], Vantelon D. [3], Guimaraes E. [2], Monvoisin G. [1], Nouet J. [1], Ponzevera Emmanuel [4], Quantin C. [1]

[1] UMR 8148 GEOPS, Université Paris Sud – CNRS – Université Paris Saclay, 91405 Cedex, France
[2] UnB, IG/GMP-ICC Centro, Campus Universitário Darcy Ribeiro, 70910-970, Brasilia-DF, Brazil / Laboratoire Mixte International, LMI OCE « Observatoire des changements Environnementaux », Institut de Recherche pour le Développement / University of Brasilia, Campus Darcy Ribeiro, Brasilia, Brazil
[3] Synchrotron Soleil, L'Orme des Merisiers, Saint Aubin, BP 48, F-91192 Gif-sur-Yvette Cedex, France
[4] IFREMER, Centre de Brest, Unité Géosciences Marines, 29280 Plouzané, France

* Corresponding author : G. Ratié, email address : gildas.ratie@gmail.com

Abstract :

Ultramafic (UM) rocks are known to be nickel (Ni) rich and to weather quickly, which makes them a good candidate to look at the Ni isotope systematics during weathering processes at the Earth's surface. The present study aims at identifying the Ni solid speciation and discussing the weathering processes that produce Ni isotope fractionation in two deep laterite profiles under tropical conditions (Barro Alto, Goiás State, Brazil). While phyllosilicates and to a lower extent goethite are the main Ni-bearing phases in the saprolitic part of the profile, iron (Fe) oxides dominate the Ni budget in the lateritic unit. Nickel isotopic composition (δ60Ni values) has been measured in each unit of the regolith, i.e., rock, saprock, saprolite and laterite (n=52). δ60Ni varies widely within the two laterite profiles, from -0.10 ± 0.05‰ to 1.43 ± 0.05‰, showing that significant Ni isotope fractionation occurs during the weathering of UM rocks.

Overall, our results show that during weathering, the solid phase is depleted in heavy Ni isotopes due to the preferential sorption and incorporation of light Ni isotopes into Fe oxides; the same mechanisms likely apply to the incorporation of Ni into phyllosilicates (type 2:1). However, an isotopically heavy Ni pool is observed in the solid phase at the bottom of the saprolitic unit. This feature can be explained by two hypotheses that are not mutually exclusive: i) a depletion in light Ni isotopes during the first stage of weathering due to the preferential dissolution of light Ni-containing minerals, and ii) the sorption or incorporation of isotopically heavy Ni carried by percolating waters (groundwater samples have δ60Ni of 2.20 and 2.27‰), that were enriched in heavy Ni isotopes due to successive weathering processes in the overlying soil and laterite units.

Keywords : Nickel cycle, lateritic regolith, nickel isotopes, XANES, ultramafic environment, weathering

1. Introduction

The characterization of Ni transfer fluxes in UM environments, which are among the main continental reservoirs of Ni (Guillot and Hattori, 2013), is crucial to better understand Ni cycling at the Earth's surface. The chemical weathering of ultramafic rock outcrops leads to the dissolution of primary ferromagnesian minerals with intense leaching of soluble major elements (like Mg and Si), and remobilization and/or reprecipitation of less soluble such as Fe, Cr, Co, and Ni in secondary minerals. Intense weathering may lead to the formation of supergene ore deposits like those found in Brazil, New Caledonia, Philippines and Dominican Republic (e.g., Trescases et al., 1981; Colin et al., 1990; Gleeson et al., 2003; Freyssinet et al., 2005; Butt and Cluzel, 2013). These formations are mainly controlled by both climatic and topographic conditions (Golightly, 1981; Freyssinet et al., 2005; Golightly, 2010; Vasconcelos et al., 2015) and result in the creation of weathering profiles, with several units that can be distinguished based on their depth and their mineralogical and geochemical compositions.

Metal stable isotope systematics provide a useful tool for tracing metal sources and cycling in natural environments (Bullen, 2014; Wiederhold, 2015), which can be used to better understand and quantify the fate of metals in the rock–soil–water–plant continuum, i.e., at the scale of the Earth's Critical Zone (CZ). To target Ni fluxes in UM environments, the specific key steps of Ni isotope fractionation and the influence of the mixing of various sources or interfacial processes, such as sorption, complexation, dissolution or precipitation, must be fully understood and characterized. Recently, Elliot and Steele (2017) published a review on the isotope geochemistry of Ni. Since the pioneering work of Cameron et al. (2009) on the preferential assimilation of light Ni isotopes by methanogens, large variations in Ni

isotope compositions (i.e., the $^{60}Ni/^{58}Ni$ ratio, which is expressed as $\delta^{60}Ni$ in ‰) have been reported in geological samples as well as in anthropogenic materials. The $\delta^{60}Ni$ values of igneous rocks range from −0.13 to 0.36‰, whereas riverine dissolved Ni has heavier Ni isotope compositions ($\delta^{60}Ni$ = 0.29 to 1.34‰), which is consistent with the relatively heavy Ni isotopic composition of the Ocean (average $\delta^{60}Ni = 1.44 \pm 0.15$‰, n = 30, Cameron and Vance, 2014). The dissolved Ni in both rivers and Oceans is isotopically heavy compared to the Bulk Silicate Earth, whose isotopic composition has been first estimated at 0.05 ± 0.05‰ (Gueguen et al., 2013) and recently reevaluated at 0.23 ± 0.08‰ (Gall et al., 2017).

To explain the relatively heavy Ni isotope composition of the Ocean and Fe-Mn crusts (the main Ni output from the Ocean; average $\delta^{60}Ni = 1.74 \pm 0.59$‰, n = 126, Gall et al., 2013; Gueguen et al., 2016), the overall input of Ni to the Ocean must be isotopically heavy. Recently, Vance et al. (2017) suggested that the heavy Ni isotope composition of the oceanic dissolved pool is the result of the sequestration of light isotopes to sulfides in anoxic and organic-rich sediments. However, the sequestration of isotopically light Ni by iron oxide has also been observed on continents (Estrade et al., 2015; Ratié et al., 2015; Wasylenki et al., 2015, Wang and Wasylenki, 2017). Until now, only a few samples of soils, weathered UM rocks and UM rocks have been analyzed (Gall et al., 2013; Gueguen et al., 2013; Estrade et al., 2015; Ratié et al., 2015; Ratié et al., 2016; Gall et al., 2017). These samples include serpentinized UM rocks (with $\delta^{60}Ni$ values ranging from 0.08 to 0.32‰), saprolitic and lateritic samples (with $\delta^{60}Ni$ values ranging from −0.61 to 0.32‰) and soil samples (with $\delta^{60}Ni$ values ranging from −0.33 to 0.11‰). The $\delta^{60}Ni$ values of sulfide mineralizations present in the serpentinite ores from two mines in Zimbabwe range from −0.47 to −0.28‰ (Hofmann et al., 2014). As a general observation, secondary minerals that form during weathering seem to have relatively light Ni isotope compositions, with $\Delta^{60}Ni_{Soil-Bedrock} = -0.47$‰ in the Barro Alto UM deposit (Ratié et al., 2015) and $\Delta^{60}Ni_{Soil-Bedrock} = -0.63$‰ in the two soil profiles that developed on Albanian serpentinized peridotite (Estrade et al., 2015). The observed depletion in heavy Ni isotopes is associated with a strong mineralogical evolution along the weathering and soil profiles. Indeed, the formation of Ni-bearing clay minerals and Fe oxides appeared to lead to the depletion of Ni heavy

isotopes, which indicates that heavy Ni isotopes are preferentially exported downwards in their dissolved form. This result is consistent with the Ni isotopic signatures measured in the exchangeable pool of the solid phase (with $\Delta^{60}Ni_{exch\text{-}total}$ values of up to 0.47‰) (Ratié et al., 2015) and with the heavy Ni isotope composition of surface water in Barro Alto (Ratié et al., 2016). Moreover, the DTPA-extractable soil fraction (i.e., the fraction associated with the solid phase, which is potentially transferred to the soil solution) exhibits heavier $\delta^{60}Ni$ values than rhizospheric soils, with values of $\Delta^{60}Ni_{Ni\ available\text{-}rhizo\ soil}$ ranging from 0.32 to 0.89‰ (Estrade et al., 2015).

Although Ni possesses different oxidation states, it is essentially present in the +II state in nature (Baes and Mesmer, 1976). Consequently, isotope fractionation is dominantly caused by various non-redox biological and physico-chemical reactions within weathering profiles, particularly isotopic partitioning between aqueous species in solution and/or fractionation occurring between dissolved and adsorbed Ni at the solid-solution interface or during the incorporation of Ni in the solid (Fujii et al., 2011; Fujii et al., 2014).

Thus, it is crucial to understand the present-day controls on the $\delta^{60}Ni$ values of both the dissolved and solid materials being transported through the CZ to infer present and past Ni cycling as well as the associated biogeochemical processes at the Earth's surface (e.g., secondary mineral formation, sorption onto minerals, organic matter complexation and plant uptake). In this study, the measured Ni isotopic compositions in two weathering profiles representative of the Barro Alto deposit (Goiás State, Brazil) have been combined with the identification of Ni solid speciation by both electron microscopy and X-ray Absorption Near Edge Structure (XANES) quantification in order to characterize the variability in Ni solid speciation that may influence Ni isotope fractionation (Schauble, 2004).

2. Materials and methods

2.1. Site description and sampling

The Barro Alto complex, along with the Niquelândia and Cana Brava complexes, is part of the Brasilia Fold Belt, which is exposed in central Brazil (De Moares and Fuck, 2000). The Barro Alto complex is a layered mafic–ultramafic intrusion that was subjected to granulite-facies metamorphism during the

Neoproterozoic (Ferreira Filho et al., 2010). The geology of the upper series of the complex is characterized by the predominance of gabbro and anorthosite. The lower series comprise two distinct segments: a lower mafic zone, which is mainly composed of gabbronorite, and a UM zone, which is mainly composed of serpentinized peridotite (Ferreira Filho et al., 2010). Trescases et al. (1981) and Baeta Jr. (1986) defined the different units of these weathering profiles as comprising serpentinized peridotite, saprolitic and lateritic units, as well as local intervals of chalcedony.

The topography of the Barro Alto complex (Goiás State, Brazil) is characterized by a succession of hills and valleys with altitudes ranging from 750 m to 1,100 m that dominate a large plain (i.e., a Velhas Surface) (De Oliveira et al., 1992). The climate is a savanna climate with dry winter (Aw), according to the Köppen-Geiger climate classification. Indeed, the average temperature at Barro Alto is 24.7°C, and the annual rainfall (1524 mm) is divided into a dry season that lasts from May to September and a wetter season that lasts from October to April. The vegetation is dominated by herbaceous plants and bushes in the UM area, which is typical of the Cerrado.

These UM zones represent a large Ni economical resource that has been exploited by the Anglo American Company since 2007; the Barro Alto deposit contains an estimated 112 million tons of nickel reserves. These nickel ores have been classified into three categories by the mining company based on their Ni and Fe contents and their SiO_2/MgO ratios: Plain Type Ore (PTO; 1.3 wt% Ni; 21 wt% Fe; SiO_2/MgO 1.7), East Type Ore (ETO; 1.6 wt% Ni; 15 wt% Fe; SiO_2/MgO 1.6) and West Type Ore (WTO; 1.8 wt% Ni; 19 wt% Fe; SiO_2/MgO 3.1). The last ore contains large amounts of chalcedony. The studied area in the Barro Alto complex is an open pit mine where weathering horizons are erratically distributed and where complete weathering profiles, similar to those commonly described in the literature, are extremely rare.

The present study focuses on two lateritic profiles of the same regolith (RC: S15°5'51.598", W49°1'1.636" and BA: S15°5'50.431, W49°0'59.405) in the Barro Alto deposit (Fig. 1). The overburden (0-3 m) was removed to facilitate drilling by the mining company. Therefore, the cores start at a depth of 3 m and were dug obliquely at the edge of a high-elevation plateau (approximately 990 m above sea level). Both the RC and BA profiles mainly comprise WTO, featuring strong

silicification in the form of chalcedony, and are therefore representative of the lateritic regolith developed at Barro Alto. For both profiles, chipped samples, provided by the geology department of the Anglo American Company, were obtained at intervals of 1 m; they are named RC 0-1 to 27-28 and BA 0-1 to 23-24. The deepest samples, which contain the typical minerals of serpentinized UM rocks (see results section), were determined to be the least weathered samples and are thus considered to represent the parent composition. An UM rock sample (serpentinite) was collected in the field close to the studied area in order to illustrate the diversity of UM rocks in this area. Moreover, groundwater samples were collected downstream of the profiles from two piezometers installed in the Barro Alto area (PZ1: S15°6'3.798", W49°1'49.004" and PZ2 S15°6'33.07", W49°1'31.457") in 2014 (winter, dry season) and 2015 (summer, rainy season) at a depth of 24 m (Fig. 1). The water samples were filtered through 0.45 µm membrane filters in the field.

2.2. Sample preparation

2.2.1. Sample digestion

Each cutting sample was homogenized and finely crushed prior to acid digestion, and all of the reagents were of analytical grade. Approximately 100 mg of the sample powder were transferred to Teflon vessels, digested with 5 mL of concentrated HF and 1.5 mL of $HClO_4$ at 180°C, and then evaporated to dryness. They were subsequently digested in a mixture of concentrated HNO_3-HCl (1.25 mL of HNO_3 and 3.75 mL of HCl) at 150°C and evaporated to dryness. Then, they were digested in concentrated HNO_3 once or twice to dissolve fluoride complexes that could have formed during the first digestion steps. For concentration measurements, which were performed using atomic absorption spectrometry (AAS), aliquots of the samples were evaporated to dryness and taken up with 0.5 M HNO_3. Another aliquot dedicated to Ni isotope analysis was taken up with 6 M HCl for the chemical separation/purification step of Ni in a clean lab.

2.2.2. Chemical separation of nickel

The Ni chemical purification procedure of the samples is based on a two-step chromatography separation procedure, which is fully described in Ratié et al. (2015). A first set of ion-exchange chromatography columns is filled with 2 mL (wet volume) of AG1-X8 anionic resin in 6 M HCl

(BioRad 100-200 mesh). This resin retains Fe, Zn and a high amount of Co and Cu (Moynier et al., 2007), while Ni remains in solution. Before the second chromatography column, a Ni double spike (^{61}Ni and ^{62}Ni) is added to the samples with a spike/natural ratio of 1 (Gueguen et al., 2013). The second set of ion-exchange chromatography columns uses a specific Ni-resin (Eichrom) composed of polymethacrylate containing a dimethylglyoxime (DMG) molecule that retains Ni on the resin as an insoluble Ni-DMG complex at pH values of 8-9. The eluted Ni solution is evaporated and taken up in 2% HNO_3.

2.3. Geochemical analyses

2.3.1. Concentration measurements

The measurements of cation contents were performed using AAS (Varian, AA240FS, Fast Sequential Atomic Absorption Spectrometer, GEOPS-Université Paris Sud). The accuracy of AAS measurements was controlled using standard solutions (EPL3, EPH3, and ESH2 from SCP Sciences) and was always better than 8% relative standard deviation (RSD) with respect to certified values. Two elements (Ti and Co) were analyzed using ICP-OES (HORIBA Jobin Yvon 2000) at the METIS laboratory (UPMC, Paris, France).

The cation exchange capacity (CEC) of all samples were determined using the Hexamine cobalt (III) method (Aran et al., 2008). After undergoing exchange with $Co(NH_3)_6^{3+}$ ions, the CEC was measured spectrometrically at 472 nm (Cary 50 UV Vis spectrophotometer, Varian). Additionally, the Ni contents were measured using AAS. The extracts were evaporated and digested with concentrated acids (see above); then, the exchangeable Ni isotopic compositions of several samples were measured (i.e., RC 15-16, RC 16-17, RC 17-18 and RC 19-20), because the exchangeable Ni contents were too low for the others.

2.3.2. Ni isotopic measurements by MC-ICP-MS

Nickel isotope ratios were measured using a Neptune (Thermo-Electron) MC-ICP-MS at the Pôle Spectrométrie Océan (PSO) of IFREMER (Centre de Brest, France). The samples and standards were introduced via an ApexQ (desolvating nebulizer, 50-75 V per µg/mL) in 0.28 M HNO_3. A single “run”

consisted of one block of 40 measurements. During each measurement, the Ni concentration (spike + natural) in the sample was 200 µg/L (optimum precision is obtained at spike/sample ratios between 0.7 and 8, Gueguen et al., 2013). The double-spike calculation procedure used to determine the true isotope ratios of the samples was based on the method described by Siebert et al. (2001) for Mo isotope determination (and developed by O. Rouxel for Ni isotope determination). This method consists of determining the corrected isotopic ratio and instrumental mass bias through iterative calculations (Albarède and Beard, 2004; Quitté and Oberli, 2006; Cameron et al., 2009). In addition, each sample analysis was bracketed by measurements of the spiked Ni standard NIST SRM 986 solution, which had the same concentration and the same spike/standard ratio as the sample. The resulting δ^{60}Ni ratios were expressed in per mil and normalized to the average value of the SRM-986 bracketing standard (Eq. A.1) (Gramlich et al., 1989).

$$\delta^{60}Ni = \left(\frac{\left(\frac{^{60}Ni}{^{58}Ni}\right)_{sple}}{\left(\frac{^{60}Ni}{^{58}Ni}\right)_{std}} - 1 \right) \times 1000 \qquad \text{Eq. (A.1)}$$

The long-term analytical sample reproducibility of the Ni standard NIST SRM 986 was ± 0.05‰ (2SD, n = 320). The average δ^{60}Ni reproducibility of sample after full chemically procedure was determined by measurement of two samples four times each (purification and measurement). This reproducibility was better than 0.03‰. Although every sample was measured three to four times, here (in figures and tables), we only report the average values and their 2 SD values calculated from replicate measurements. Note that a 2 SD of 0.05‰ (external reproducibility) was reported when the calculated 2 SD was less than 0.05‰. A procedural blank sample was included within every batch of samples. The blanks had an average amount of 17 ng of Ni (n = 8), which is negligible relative to the amount of Ni that was processed for each sample (usually 8-10 µg of Ni).

2.4. Mineralogical characterization

2.4.1. X-ray diffraction

The mineralogical compositions of these samples were determined by X-ray diffraction (XRD), using either a PANanalytical XRD (at the University Paris Sud, France) or a RIGAKU Ultima IV

diffractometer (at the University of Brasilia, Brazil). The XRD patterns were obtained for finely crushed powders (<2 mm fraction) and clay fractions (< 2 µm). The clay fraction was separated by centrifugation and clay mineralogy determined on oriented air-dried, ethylene glycol solvated and heated (500°C for 3h) material. The PANanalytical diffractometer used a Ni-filtered Cu-Kα radiation with an operating voltage of 45 kV; a beam current of 40 mA; a step size of 0.0167° 2θ with a counting time of 55 s per step; and a scanning range of 3 to 80° 2θ. The RIGAKU diffractometer used a Ni-filtered Cu-Kα radiation and graphite monochromator with an operating voltage of 45 kV; a beam current of 15 mA; and a scanning speed of 2°/min between 2 and 80° 2θ.

2.4.2. Electron microscopy

Backscattered electron images of a selection of lateritic and saprolitic samples were obtained using a Philips XL30 scanning electron microscope (SEM) operating with a beam voltage of 15 kV and a beam current of 1.5 µA, equipped with an energy dispersive X-ray spectrometer (EDX-PGT Ge-detector; acquisition time 40 s, GEOPS laboratory). Particles were also imaged with a JEOL JEM-2010 LaB6 TEM operating at 200 kV (CINaM Laboratory, University of Aix-Marseille, France). A sample aliquot was suspended in a few mL of ethanol and sonicated for 5 min. A drop of suspension was then evaporated on a carbon-coated copper grid (200 mesh/100 µm) placed on filter paper. Elemental spectra were determined using EDS (Bruker QUANTAX system). The analyses were carried out in nanoprobe mode with a probe diameter of 10–20 nm and an acquisition time of 40 s.

2.5. X-ray Absorption Near Edge Structure (XANES)

Bulk XANES spectra were collected at the Ni K-edge on the SAMBA beamline at the Soleil synchrotron (Saint Aubin, France) for references and on the XAFS2 beamline at the Brazilian Synchrotron Light Laboratory (LNLS, Campinas, Brazil) for samples; both were located on a bending magnet. References and samples were prepared as pellets of finely ground and homogenized powders and were sealed with Kapton tape. The data were collected at room temperature using a Si(111) monochromator with 2 eV, 0.1 eV and 1 eV steps in the pre- edge, edge and post-edge regions, respectively. The counting time was set at 1 s per point. The spectra were collected at room

temperature in both transmission and fluorescence modes. The incident beam energy was calibrated setting the position of the inflection point of a Ni metal foil EXAFS spectrum at 8347 eV. For each sample or reference, four to seven scans were sufficient to obtain a good signal/noise ratio. The spectra were averaged and normalized using the ATHENA code (Ravel and Newville, 2005).

Several reference compounds, selected according to XRD and SEM investigations, were analyzed: a Ni-rich serpentine (Ni 50 wt%), a Ni-poor serpentine (Ni 5 wt%) synthetized by Pr. F. Martin and collaborators (GET lab, Toulouse, France), a synthetized goethite containing Ni (Ni 1 wt%), a gem-quality olivine (Ni 0.14 wt%) kindly provided by Dr. G. Delpech (GEOPS lab). The spectrum of Ni-rich synthetic talc (Ni 50 wt%) was kindly provided by Dr. A. Dumas (Dumas et al., 2015) and the spectrum of trevorite ($NiFe_2O_4$) was provided by Dr. K. Tirez from VITO, Belgium (Tirez et al., 2011).

The relative speciation of Ni in the samples was determined by Linear Combination Fits (LCF). LCF reconstruct the sample spectrum using a combination of selected model spectra (i.e., reference compounds) and report the goodness of fit parameter (R-factor) along with the percent that each model contributes to the fit. LCF were performed on the normalized spectra of the samples in the energy range of 8327-8382 eV, not forcing the weights to sum to 1, using the ATHENA software (Ravel and Newville, 2005).

3. Results

3.1. Geochemical and mineralogical descriptions of the profiles

The geochemical and mineralogical compositions of the RC (n = 28) and BA profiles (n = 24) are summarized in Tables 1 and 2. A depletion in Mg and enrichment in Fe are observed during the weathering processes for both profiles (Fig. 2). The deepest core samples, which are considered to be saprock samples (RC 26-27, RC 27-28, BA 22-23 and BA 23-24), have relatively large Mg contents (15.6-19.7 wt%), Si contents that are close to 20 wt% and Ni contents of 2.7-3.5 g kg^{-1} (Tables 1 and 2). Their mineralogical assemblage comprises primary minerals, i.e., serpentine, chlorite, amphibole,

olivine and traces of quartz (Tables 1 and 2, Fig. EA-1). The serpentinite collected in the vicinity of the core location exhibits large Mg contents (24 wt%) and is mainly composed of serpentine.

Saprolite samples (RC 15-16 to RC 25-26, BA 11-12 to BA 12-13 and BA 16-17 to BA 21-22) are characterized by large Mg contents, which decrease from the bottom to the top of the unit (Fig. 2); in contrast, the Fe and Ni contents (up to 13.7 wt% and 37.4 g kg^{-1}, respectively) increase from the bottom to the top of the unit. These samples contain serpentine, chlorite, talc, smectite, goethite, magnetite and quartz. Additionally, a level enriched in smectite was found only in the upper part of the saprolitic unit of the RC profile (RC 15-16 and RC 16-17).

The lateritic unit (RC 0-1 to RC 14-15, BA 0-1 to BA 10-11and BA 13-14 to BA15-16) is characterized by low Mg contents (< 3.6 wt%) and high Fe contents (up to 17.5 wt%). The nickel content is lower than in saprolite, and it varies from 1.7 to 11.3 g.kg^{-1} in the RC profile and from 1.9 to 14.5 g kg^{-1} in the BA profile. The mineralogy is dominated by Fe oxides (both goethite and hematite) and quartz, as well as traces of serpentine and chlorite. Both lateritic profiles, particularly the BA one, are strongly silicified. This silicified part of the laterite exhibits large Si concentrations (up to 43.0 wt%) and very low contents of other major and trace elements (Tables 1 and 2, Fig. EA-1).

The cation exchange capacity measured in the RC samples ranges from 0.7 to 59.3 $cmol_c$/kg and is particularly high (55.3 to 59.3 $cmol_c$/kg) in the upper part of the saprolite, which is rich in smectite (at depths of 15-17 m) (Table 3). In the lateritic unit, the CEC ranges from 2.2 to 4.5 $cmol_c$/kg. Exchangeable Ni accounts for 7.4 - 9.1% of the total Ni in the upper saprolite and only 0 - 0.2% of the total Ni in the lateritic unit.

The water samples (< 0.45 µm) collected in two piezometers in 2014 (dry season) and 2015 (rainy season) have high pH values (7.5-9.3) and are Si and Mg rich and Ca and K poor (Table 4). Their Mg/Ca ratios are characteristic of UM draining waters, with a mean value of 11.7 ± 3.4. Their Ni concentrations range from 7.0 to 59.0 µg/L.

3.2. Ni content in minerals by electron microscopy

The SEM and TEM-EDS observations led to the identification of Ni-bearing minerals, which are mainly serpentine, smectite and goethite (Fig. 3). The RC 20-21 sample (saprolitic unit) exhibits Ni concentrations ranging from 2.2 to 3.2 wt% for serpentine (n=6), which present different morphologies, corresponding to the presence of both lizardite and chrysotile. In the upper saprolite unit (RC 16-17), smectite and goethite contain up to 3.3 wt% and 3.1 wt% Ni, respectively. In the lateritic unit (RC 4-5), goethite contains appreciable amounts of Ni (3.0 wt%), while serpentine contains 1.3 wt% Ni.

3.3 Nickel speciation by XANES

The normalized Ni K-edge XANES spectra collected on relevant reference compounds and on selected RC samples (n = 14) are represented in Figure 4a and 4b, respectively. References spectra exhibit a white line with two features at about 8350 eV (peak A) and 8352 eV (peak B) followed by a shoulder at 8357 eV and a broad oscillation around 8365 eV. The position of this oscillation (doubled in olivine) is related to multiple scattering of the first atom neighbors around Ni and varies according to the nickel – neighbor distance. The peak A and B relative intensity varies according to the host Ni phase nature. In phyllosilicates, serpentines and talc, peak A occurs as a shoulder, while in olivine and goethite peak B occurs as a shoulder. In trevorite, peak A and B merge into a single peak pointed around 8351 eV. In all spectra, a pre-edge (peak C) occurs before the white line at 8333 eV. In all the references, Ni is octahedrally coordinated and the pre-edge peak is assigned to the 1s 3d transitions for Ni in octahedral symmetry. The additional pre-edge peak in trevorite (peak D at 8335 eV) is assigned to 1s 3d transitions for Ni located in tetrahedral symmetry which occurs also in the spinel structure.

The XANES spectra collected for the RC samples exhibit the same features as the ones from the references: a white line with peaks A and B centered at the same position, a shoulder around 8357 eV and a broad peak at 8365 eV. The single pre-edge peak centered at 8333 eV evidences that in all the samples the Ni coordination is mainly octahedral. The XANES spectra in all samples analyzed in the saprolitic and saprock unit of the RC profile (except RC 17-18) exhibit similar shape than the Ni-reference phyllosilicates, i.e. peak A occurring as a shoulder, highest intensity of peak B. Concerning

spectra of RC 0-1, RC 3-4, RC 8-9 and RC 17-18, their broad white line maxima suggest that they are provided by a mixture of phases in which the presence of Ni-goethite (i.e. increases of peak A) is higher in lateritic samples. Thus, the Ni speciation in those RC samples can be considered as a mixture of the relevant Ni-bearing reference phases, consistent with the phases identified by XRD and SEM-EDS.

A linear combination fit (LCF) was performed for all of the spectra using Ni reference compounds (Fig. 5 and Table EA-1). The LCF totals reach up to 99%, indicating that the reference spectra adequately characterize the analyzed samples. The LCF shows that the main Ni-bearing phases are goethite and phyllosilicates (represented by serpentine and talc). Nickel-bearing talc was used in the LCF in order to evaluate the contribution of structural Ni in 2:1 phyllosilicates (either talc, trioctahedral smectite or Ni-containing dioctahedral smectite). Its contribution is particularly high in samples RC 15-16 and 16-17 (almost 30%), where smectite is particularly abundant (Table 1), but it is also high in RC 18-19 and 19-20, where talc was found by XRD together with smectite in the clay-sized fraction (Table 1). The contribution of Ni-goethite increases toward the surface, while the contribution of Ni-poor serpentine decreases. In the deepest sample (RC 27-28), 16% of Ni is associated with goethite, while more than 70% of Ni is associated with goethite in the lateritic samples.

3.4 Nickel isotopic compositions of the profiles

The δ^{60}Ni values of the RC and BA profile samples range from -0.10 ± 0.05‰ to 1.43 ± 0.05‰ (Tables 1 and 2). The Ni isotopic signatures show different trends in the two profiles (Fig. 2). In the BA profile, δ^{60}Ni values oscillate between -0.10 ± 0.05‰ and 0.77 ± 0.10‰, while in the RC profile, this variation is much larger (from -0.04 to 1.43‰). However, both profiles, the heaviest Ni isotope compositions are found at the bottom of the saprolite, above the saprock samples (1.43 ± 0.05‰ for RC and 0.77 ± 0.10‰ for BA). Serpentinite yields a δ^{60}Ni value of 0.10 ± 0.06‰.

In the RC profile, saprock exhibits a mean δ^{60}Ni value of 0.31‰. The δ^{60}Ni values of the saprolitic unit vary from -0.04 to 1.43‰; the smectitic zone is characterized by a light Ni isotopic signature (from -0.04 to 0.03‰), while the bottom part is dominated by serpentine, which presents heavier δ^{60}Ni

values of up to 1.43‰. The exchangeable nickel fractions measured in four samples exhibit δ^{60}Ni values ranging from 0.26 ± 0.16 to 0.96 ± 0.05‰, while the δ^{60}Ni values of the solid residue, i.e., after extraction, range from -0.13 ± 0.07 to 0.28 ± 0.09‰ (Table 3). The Ni isotopic mass balance is respected in quantitative terms.

The lateritic unit, which is strongly silicified, records a smaller range of δ^{60}Ni values than the saprolitic unit, ranging from 0.03 to 0.70‰. The heaviest δ^{60}Ni values are found at the top and bottom edges of the unit, while the lightest δ^{60}Ni values are found in the middle of the chalcedony vein. In the BA profile, saprock exhibits a mean δ^{60}Ni value (0.25‰) that is similar to that of the RC saprock samples. The δ^{60}Ni values of the saprolitic unit are also variable, ranging from -0.10 to 0.77‰. The silicified laterite (where chalcedony is predominant) presents a smaller range of δ^{60}Ni variations than the saprolitic units, ranging from 0.05 to 0.27‰.

Finally, the groundwater samples display heavy δ^{60}Ni values of 2.27 ± 0.08‰ and 2.20 ± 0.09‰ (Table 4).

4. Discussion

4.1. Evolution of Ni speciation during weathering: the role of goethite and phyllosilicate in Ni scavenging

The combination of XRD, TEM-EDS and XANES techniques shows the major evolution of Ni speciation during the weathering of serpentinized ultramafic rock. The Barro Alto deposit is dominated by two types of Ni-bearing minerals, i.e., Mg phyllosilicates and Fe oxides. In the parent material, i.e., partially serpentinized UM rock, Ni is mainly included in serpentine and chlorite, together with forsterite-olivine (Ratié et al., 2015). The weathering of those minerals leads to the release of mobile elements such as Mg, Si and Ni, which further contribute to the formation of secondary minerals such as clay minerals in the saprolite unit. Iron is rapidly oxidized and then precipitates as Fe-oxides or, to a much lower extent, incorporated in the phyllosilicate lattice. In the saprolitic samples, the occurrence of Ni-bearing goethite, which hosts a large proportion of Ni, confirms that goethite starts forming in the early stage of weathering and efficiently scavenges Ni, as

previously observed by Trescases (1979) and Dublet et al. (2012). SEM-EDS and quantitative XANES analyses show that both Ni-rich and Ni-poor serpentine are involved in Ni scavenging. Ratié et al. (2015) reported that talc and sepiolite (two 2:1 phyllosilicates) can also be Ni-bearing phases in the UM complex of Barro Alto.

Iron oxides and Mg silicates have been shown to carry significant proportions of Ni in UM deposits worldwide, like in New Caledonia (Trescases, 1975; Becquer et al., 2006; Wells et al., 2009; Dublet et al., 2012; Fritsch et al., 2016), Brazil (Trescases et al., 1981; Colin et al., 1990; De Oliveira et al., 1992), the Philippines (Fan and Gerson, 2011), Colombia (Gleeson et al., 2004) Australia (Elias et al., 1981; Gaudin et al., 2004), and the Dominican Republic (Aiglsperger et al., 2016; Roqué-Rosell et al., 2016; Villanova-de-Benavent et al., 2016). The mass transfer coefficient for Ni (Figure EA-2) shows that most samples from the upper part of the profiles are depleted in Ni relative to the deepest core sample (RC 27-28 and BA 23-24). On the opposite, saprolitic samples are strongly enriched in Ni relative to the deepest ones. Accordingly, one can consider that the vertical distribution of Ni along both studied profiles is driven by the classical weathering scheme. Besides, lateral circulation of fluids may increase the Ni enrichment observed in the saprolitic part.

The largest Ni contents (up to 37.40 g kg^{-1} for BA 11-12) were measured in the upper part of the saprolite, particularly in the RC profile, where smectite is present in large amounts. Nickel can be located in the octahedral sheets of smectite layers (Gaudin et al., 2005; Raous et al., 2013) and in exchangeable positions (Raous et al., 2013). The quantitative analysis of the XANES spectra of the RC15-16 and RC16-17 samples, which contain significant amount of smectite, shows that approximately 30% of Ni is structurally scavenged in the octahedral layer of 2:1 phyllosilicates for these samples.

In the lateritic samples, Ni is mainly associated with Fe oxides that scavenge 54 to 78% of Ni (Fig. 5), while 7-26% of Ni is associated with Ni-poor serpentine. The predominant Ni incorporation into goethite within the lateritic ore examined here is in agreement with New Caledonian and Indonesian nickel laterites, where 78 ± 7% and 58 ± 15% of Ni was found to be associated with goethite (Dublet et al., 2012; Fan and Gerson, 2015). However, these results are significantly different from those

obtained in a Philippine limonite, where only 40 ± 10% of Ni was incorporated into goethite (Fan and Gerson, 2011). Finally, Mn oxides were neither detected by XRD nor observed by other techniques, and they are therefore not considered as significant Ni scavengers. From the saprolitic to the lateritic unit, the Ni content decreases for both profiles (Tables 1 and 2), emphasizing the mobility of this element during weathering, either during the dissolution of the phyllosilicate pool or during the exclusion of Ni from goethite through successive dissolution / recrystallization cycles, as observed in New Caledonia by Dublet et al (2015).

4.2. Nickel isotope signatures of the solids in the Barro Alto UM system

The average δ^{60}Ni value of the saprock and serpentinite samples (i.e., parent material) is 0.24 ± 0.08‰ (n= 5). This value is similar to the recent estimate of average δ^{60}Ni for the Bulk Silicate Earth (BSE) at 0.23 ± 0.08‰ (Gall et al., 2017), but heavier than former estimates that proposed an average value of 0.05 ± 0.05‰ (Gueguen et al., 2013). Our average δ^{60}Ni value is also similar to that of Albanian serpentinized peridotites (δ^{60}Ni = 0.25 ± 0.16‰, 2SD, n = 2) reported by Estrade et al. (2015). Published δ^{60}Ni data on UM rocks and our dataset show a small range of variation suggesting that the serpentinization process does not significantly affect the δ^{60}Ni values of peridotites (Gall et al., 2013; Gueguen et al., 2013; Chernonozkhin et al., 2015; Estrade et al., 2015; Ratié et al., 2015; Gall et al., 2017).

In contrast, a wide range of δ^{60}Ni is found in the regolith, especially in the saprolite, with values ranging from -0.10 ± 0.05‰ to 1.43 ± 0.05‰. The lateritic parts of the profiles show a less pronounced variability with δ^{60}Ni values ranging from 0.03 ± 0.05‰ to 0.70 ± 0.05‰. The large number of samples analyzed here (n = 52) allowed us to evidence this strong variability in δ^{60}Ni at the regolith scale, which was not observed in previous studies due to the limited number of samples per site (Gall et al., 2013; Ratié et al., 2015). However, the present range of variation does not encompass the full range of published δ^{60}Ni values in solid materials, with the lightest and heaviest ones published so far at -0.61 ± 0.03‰ for a sample from another outcrop in the Barro Alto deposit (Ratié et al., 2015) and 2.83‰ for a clinopyroxene in lherzolite from Cameroon (Gall et al., 2017). Soils that have developed on UM rocks analyzed so far constantly show lighter δ^{60}Ni signature than parent rocks

(or BSE), under both tropical conditions (from -0.26 ± 0.08‰ to 0.11 ± 0.10‰; Ratié et al., 2016) and temperate conditions (from -0.33 ± 0.11‰ to -0.01 ± 0.11‰; Estrade et al., 2015). Apart from the 2.83‰ value reported recently by Gall et al. (2017) for a sample from Cameroon, no other work to our knowledge has reported such heavy δ^{60}Ni for continental solids (up to 1.43‰ for a deep saprolitic sample). Up to now, heavy δ^{60}Ni (i.e. higher than BSE) were exclusively attributed to the dissolved phase of rivers and Oceans, as well as marine sediments and Fe-Mn crusts (Gall et al., 2013; Cameron and Vance, 2014; Porter et al., 2014; Gueguen et al., 2016; Vance et al., 2016; Vance et al., 2017).

4.3. Nickel isotope fractionation during weathering: the role of secondary minerals

The weathering of UM rocks releases into percolating water highly soluble elements such as Mg and Si, and to a lower extent Ni that is less mobile. In contrast, Fe and Mn are quickly oxidized and reincorporated into oxides. Continuous weathering of the still evolving laterite leads to a vertical stratification of the profile in terms of mineralogy and geochemical signature (both elemental and isotopic). The extent of UM rock weathering can be tracked with the Mg/Ni ratio (Fig. 6, and Ratié et al., 2015) and in a less straightforward way, with Ni isotopes in the solid matrix (Fig. 6).

As mentioned in section 3.1, each profile can be divided in three units, i) the lateritic unit, ii) the saprolitic unit and iii) the saprock. Although lacking due to mining activity needs, the soil has to be considered in order to understand the full geochemical and isotopic history of the investigated profiles. To do so, we use soil data from the same regolith already published in Ratié et al (2015 and 2016). While we observe a chemical continuum from the saprock to the saprolitic unit, the lateritic part of the profiles seems to be somehow disconnected from this continuum with a much more complicated weathering history as suggested by the strong silicification of this unit in both profiles.

Within the saprolite, the upper part is expected to have experienced weathering for the longest time. In fact, the Mg/Ni ratio of the upper saprolite varies from 2 to 8, which is much smaller than in the lower saprolite (10 to 62) and the saprock (144 to 213). This lowering of the Mg/Ni ratio from the saprock to the upper saprolite is consistent with an increasing weathering intensity due to longer fluid-rock interaction. Associated to this chemical gradient we observe a change in the mineralogy of Ni-bearing

phases as well as a drastic change in δ^{60}Ni. As exemplified with the RC profile where we measured Ni speciation, Ni-poor serpentine, which is the main Ni carrier at the base of the saprolite (>40%) and in the saprock (48%), is progressively replaced by secondary goethite and phyllosilicates going upward in the saprolite, until it disappears in the upper saprolite (Fig. 5). This progressive replacement of Ni-bearing minerals is accompanied by a change in δ^{60}Ni that decreases from 0.77‰ and 1.43‰ for BA and RC profiles at the base of the saprolite, respectively, to values down to -0.08‰ and -0.04‰ for BA and RC profiles in the upper saprolite, respectively. The lightest δ^{60}Ni values correspond to the highest amounts of Ni in goethite and/or 2:1 phyllosilicates (Fig. 7). These later values are lower than the ones measured for the saprock (0.23-0.26‰ for BA and 0.28-0.32‰ for RC), suggesting preferential sorption, incorporation and co-precipitation of light Ni isotopes into Fe oxide and/or phyllosilicates. This is consistent with Wasylenki et al. (2015) and Wang and Wasylenki (2017) who have reported Ni isotopic fractionation associated with the retention of Ni in Fe oxides (ferrihydrite and hematite). The processes of adsorption and coprecipitation onto ferrihydrite lead to the preferential incorporation of lighter isotopes in the solid (Wasylenki et al., 2015), which also occurs during the transformation of ferrihydrite to hematite (Wang and Wasylenki, 2017). As a consequence of light Ni incorporation in secondary minerals, we expect an enrichment of the remaining dissolved Ni in heavy isotopes. This feature is consistent with the heavy signature of groundwater collected downstream of the profiles (2.20‰ and 2.27‰), and with published river data (Cameron and Vance, 2014).

UM soils from Barro Alto, the ultimate "residue" of chemical weathering, are dominantly composed of iron oxides and are even more enriched in light Ni isotopes (from -0.30 to 0.11‰, average of -0.13 ± 0.11‰, n = 18) than the RC and BA profiles (Ratié et al., 2015; Ratié et al., 2016).

The apparent light Ni isotope incorporation in iron oxides and/or phyllosilicates within our profiles may be related to the effect of structural parameters of iron oxides (size, morphology, porosity, surface accessibility, types of surface complexes) on Ni isotope fractionation or the possible presence of tetrahedral Ni^{2+} in addition to octahedral Ni^{2+} in the mineral lattice (Wang and Wasylenki, 2017). In solution, nickel is hexacoordinated $Ni(H_2O)_6^{2+}$ (Colpas et al., 1991; Montargès-Pelletier et al., 2008), in which Ni-O has a bond length of 2.04 Å. In the trioctahedral layer of phyllosilicates, Ni is also

octahedrally coordinated, but distortions of bond angles and length (as well as different bond strengths) occur. Dumas et al. (2015) reported a bond length of 2.06 Å for Ni-O in 50% Ni talc, while Dublet et al. (2012) reported lengths of 2.05 and 2.06 Å in Ni-poor and Ni-rich serpentines, respectively, and 2.09 Å in Ni-forsterite. According to Schauble (2004), the slight differences in bond length between the primary source of Ni (olivine) and secondary minerals could explain the preferential incorporation of light Ni in secondary minerals.

In the lower part of the saprolite, where the dominant Ni-bearing mineral is Ni-poor serpentine, we found relatively high Mg/Ni ratios (from 10 to 62) compared to the upper part of the saprolite or soils (from 1 to 10; Ratié et al., 2015; Ratié et al., 2016) and the heaviest δ^{60}Ni measured in each profile (0.77 ± 0.10‰ for BA 21-22 and 1.43 ± 0.05‰ for RC 24-25).

This feature can be explained by two concepts that are not mutually exclusive. First, due to the sorption and incorporation of light Ni isotopes into Fe oxides and phyllosilicates (2:1), the preferential leaching of the isotopically heavy Ni pool occurs in the dissolved phase to the deepest horizon. The heavy δ^{60}Ni values of the exchangeable fraction ($\Delta^{60}Ni_{exch\text{-}tot}$ = 0.26‰) and the groundwater samples (2.27 ± 0.08‰ and 2.20 ± 0.09‰) confirm that the dissolved phase is enriched in heavy Ni isotopes. During the formation of secondary serpentine in deep saprolitic samples, the isotopically heavy Ni pool could thus be incorporated in the mineral structure.

Second, two different mechanisms could explain the apparent Ni isotope fractionation observed during mineral dissolution. On the one hand, incongruent dissolution of multimineralic rocks containing various Ni-bearing phases having different dissolution kinetics could lead to the enrichment in heavy Ni isotopes in the solid phase during the first stage of weathering (Gall et al., 2017). On the other hand, kinetic isotope effect during mineral dissolution could lead to an initially light solution associated with enrichments of heavy isotopes of the remaining Ni on the surface of the dissolving minerals (Wiederhold et al., 2006 for Fe isotopes). This second mechanism is however not consistent with the heavy δ^{60}Ni signature of groundwater. But even though this effect is mainly a transient surface effect and limited in its ability to create isotopically light solutions, depending on the surface

properties of the investigated material, it could still create measurable effects, also in natural field systems during Fe detachment from the phyllosilicates (Kiczka et al., 2011).

5. Conclusions

The purpose of the present study was to identify the Ni-bearing minerals and the processes that could induce Ni isotope fractionation in two Ni-laterites collected in the Barro Alto deposit. Phyllosilicates (Ni-poor and Ni-rich serpentine, as well as smectite and talc) are the main Ni scavenging phases in the saprolitic part of the profile, while goethite is the major Ni-bearing phase in the lateritic part.

This study complements other studies on the Ni isotopic systematics in terrestrial samples. Despite their strong silicification, the two profiles studied here provide important clues that can be used to understand what happens to Ni isotopes during tropical weathering and, more specifically, in silicified oxide deposits. The parent material has a δ^{60}Ni composition similar to that of the BSE reported recently by Gall et al. (2017). The regolith samples reveal a wide range of Ni isotope compositions, ranging from -0.10 ± 0.05‰ to 1.43 ± 0.05‰, and the heaviest isotopic compositions were found in the saprolite, where a high variety of Ni-bearing phyllosilicates coexist. The overlying samples, i.e., laterite and silicified laterite, have much less variable δ^{60}Ni values that are either lighter or heavier than that of the parent material. By combining Ni isotope compositions with Ni solid speciation by XANES, we show that Ni solid speciation may influence the bulk Ni isotope composition, particularly Ni retention by Fe oxides and 2:1 phyllosilicates.

Sorption, co-precipitation and dissolution processes seem to regulate the overall Ni isotope systematics during the weathering of UM rocks. This study confirms i) the depletion in heavy Ni isotopes during the overall weathering of UM rocks, and ii) the presence of an isotopically heavy Ni pool in the solid phase at the bottom of the saprolitic unit. Two hypotheses can be proposed to explain this last observation. First, due to the sorption and incorporation of light Ni isotopes into Fe oxides and phyllosilicates (2:1), the preferential leaching of an isotopically Ni heavy pool occurs in the dissolved phase to the deepest horizon. During the formation of secondary serpentine, the isotopically Ni heavy pool could thus be incorporated in the mineral structure. Second, the heterogeneous mineralogy of the

deepest samples (up to four Ni-bearing phases) might be responsible for the preferential release of light Ni isotopes due to differences in mineral dissolution kinetics (depending on the signatures of the different minerals), as well as the necessary bond energy to break different nickel isotopes.

Acknowledgments

This work was financially supported by the French Ministry of National Education and Research (G. Ratié PhD grant), National French Program EC2CO from INSU, CNRS, and a Marie Curie International Research Staff Exchange Scheme Fellowship within the 7th European Community Framework Programme (NIDYFICS, n°318123) and CNPq universal 445423/2014-5, CNPq–PQ 310750/2014-8, FAP-DF 193.000.932/2015. This work also benefited from the Ciencia Sem Fronteiras program (C. Quantin, PV: 406288/2015-1). The authors wish to thank Anglo American for access to their field facilities, the staff for their help during sampling, and O. Rouxel (IFREMER, France) for the Ni double spike preparation. The authors wish to thank A. Baronnet and O. Grauby (CINaM, France) for their insights and for providing access to TEM facilities, as well as E. Aubry for providing access to the ICP-OES facilities at METIS laboratory. We acknowledge SOLEIL and LNLS for provision of synchrotron radiation facilities and we would like to thank E. Fonda and S.J.A. Figueroa for assistance in using SAMBA and XAFS2 beamlines, respectively. The authors thank three reviewers and Dr. Jan Wiederhold (AE) for their valuable comments and suggestions.

References

Aiglsperger, T., Proenza, J.A., Lewis, J.F., Labrador, M., Svojtka, M., Rojas-Puron, A., Longo, F., and Ďurišová, J. (2016). Critical metals (REE, Sc, PGE) in Ni laterites from Cuba and the Dominican Republic. Ore Geol. Rev. *73*, 127–147.

Albarede, F., and Beard, B. (2004). Analytical methods for non-traditional isotopes. In Geochemistry of Non-Traditional Stable Isotopes, C.M. Johnson, B.L. Beard, and F. Albarede, eds. pp. 113–152.

Aran, D., Maul, A., and Masfaraud, J.-F. (2008). A spectrophotometric measurement of soil cation exchange capacity based on cobaltihexamine chloride absorbance. Comptes Rendus Geosci. *340*, 865–871.

Baes, C.F., and Mesmer, R.E. (1976). Hydrolysis of cations (Wiley).

Baeta Jr, J.D.A., Fogaça, C.C., Ramos, J.B., Jo, J.A.G., and Barberi, M. (1978). Projeto manganês no centro-sul de Goiás. Relatório Final Goiâ. DNPMCPRM *7*, 98.

Becquer, T., Quantin, C., Rotte-Capet, S., Ghanbaja, J., Mustin, C., and Herbillon, A.J. (2006). Sources of trace metals in Ferralsols in New Caledonia. Eur. J. Soil Sci. *57*, 200–213.

Bullen, T.D. (2014). 7.10 - Metal Stable Isotopes in Weathering and Hydrology. In Treatise on Geochemistry (Second Edition), H.D. Holland, and K.K. Turekian, eds. (Oxford: Elsevier), pp. 329–359.

Butt, C.R., and Cluzel, D. (2013). Nickel laterite ore deposits: weathered serpentinites. Elements *9*, 123–128.

Cameron, V., Vance, D., Archer, C., and House, C.H. (2009). A biomarker based on the stable isotopes of nickel. Proc. Natl. Acad. Sci. *106*, 10944–10948.

Cameron, V., and Vance, D. (2014). Heavy nickel isotope compositions in rivers and the oceans. Geochim. Cosmochim. Acta *128*, 195–211.

Chernonozhkin, S.M., Goderis, S., Lobo, L., Claeys, P., and Vanhaecke, F. (2015). Development of an isolation procedure and MC-ICP-MS measurement protocol for the study of stable isotope ratio variations of nickel. J. Anal. At. Spectrom.

Colin, F., Nahon, D., Trescases, J.-J., and Melfi, A.J. (1990). Lateritic weathering of pyroxenites at Niquelandia, Goias, Brazil; the supergene behavior of nickel. Econ. Geol. *85*, 1010–1023.

Colpas, G.J., Maroney, M.J., Bagyinka, C., Kumar, M., Willis, W.S., Suib, S.L., Mascharak, P.K., and Baidya, N. (1991). X-ray spectroscopic studies of nickel complexes, with application to the structure of nickel sites in hydrogenases. Inorg. Chem. *30*, 920–928.

De Moraes, R., and Fuck, R.A. (2000). Ultra-high-temperature metamorphism in Central Brazil: the Barro Alto complex. J. Metamorph. Geol. *18*, 345–358.

De Oliveira, S., Trescases, J., and Melfi, A. (1992). Lateritic Nickel Deposits of Brazil. Miner. Deposita *27*, 137–146.

Dublet, G., Juillot, F., Morin, G., Fritsch, E., Fandeur, D., Ona-Nguema, G., and Brown, G.E. (2012). Ni speciation in a New Caledonian lateritic regolith: A quantitative X-ray absorption spectroscopy investigation. Geochim. Cosmochim. Acta *95*, 119–133.

Dublet, G., Juillot, F., Morin, G., Fritsch, E., Fandeur, D., and Brown, G.E. (2015). Goethite aging explains Ni depletion in upper units of ultramafic lateritic ores from New Caledonia. Geochim. Cosmochim. Acta *160*, 1–15.

Dumas, A., Mizrahi, M., Martin, F., and Requejo, F.G. (2015). Local and Extended-Order Evolution of Synthetic Talc during Hydrothermal Synthesis: Extended X-ray Absorption Fine Structure, X-ray Diffraction, and Fourier Transform Infrared Spectroscopy Studies. Cryst. Growth Des. *15*, 5451–5463.

Elias, M., Donaldson, M.J., and Giorgetta, N.E. (1981). Geology, mineralogy, and chemistry of lateritic nickel-cobalt deposits near Kalgoorlie, Western Australia. Econ. Geol. *76*, 1775–1783.

Elliott, T., and Steele, R.C. (2017). The isotope geochemistry of Ni. Rev. Mineral. Geochem. *82*, 511–542.

Estrade, N., Cloquet, C., Echevarria, G., Sterckeman, T., Deng, T., Tang, Y., and Morel, J.-L. (2015). Weathering and vegetation controls on nickel isotope fractionation in surface ultramafic environments (Albania). Earth Planet. Sci. Lett. *423*, 24–35.

Fan, R., and Gerson, A.R. (2011). Nickel geochemistry of a Philippine laterite examined by bulk and microprobe synchrotron analyses. Geochim. Cosmochim. Acta *75*, 6400–6415.

Fan, R., and Gerson, A.R. (2015). Synchrotron micro-spectroscopic examination of Indonesian nickel laterites. Am. Mineral. *100*, 926–934.

Ferreira Filho, C.F., Pimentel, M.M., de Araujo, S.M., and Laux, J.H. (2010). Layered intrusions and volcanic sequences in Central Brazil: geological and geochronological constraints for Mesoproterozoic (1.25 Ga) and Neoproterozoic (0.79 Ga) igneous associations. Precambrian Res. *183*, 617–634.

Freyssinet, P., Butt, C.R.M., Morris, R.C., and Piantone, P. (2005). Ore-forming processes related to lateritic weathering. Econ. Geol. 100th Anniv. Vol. *1*, 681–722.

Fritsch, E., Juillot, F., Dublet, G., Fonteneau, L., Fandeur, D., Martin, E., Caner, L., Auzende, A.-L., Grauby, O., and Beaufort, D. (2016). An alternative model for the formation of hydrous Mg/Ni layer silicates ("deweylite"/"garnierite") in faulted peridotites of New Caledonia: I. Texture and mineralogy of a paragenetic succession of silicate infillings. Eur. J. Mineral. *28*, 295–311.

Fujii, T., Moynier, F., Dauphas, N., and Abe, M. (2011). Theoretical and experimental investigation of nickel isotopic fractionation in species relevant to modern and ancient oceans. Geochim. Cosmochim. Acta *75*, 469–482.

Fujii, T., Moynier, F., Blichert-Toft, J., and Albarède, F. (2014). Density functional theory estimation of isotope fractionation of Fe, Ni, Cu, and Zn among species relevant to geochemical and biological environments. Geochim. Cosmochim. Acta *140*, 553–576.

Gall, L., Williams, H.M., Siebert, C., Halliday, A.N., Herrington, R.J., and Hein, J.R. (2013). Nickel isotopic compositions of ferromanganese crusts and the constancy of deep ocean inputs and continental weathering effects over the Cenozoic. Earth Planet. Sci. Lett. *375*, 148–155.

Gall, L., Williams, H.M., Halliday, A.N., and Kerr, A.C. (2017). Nickel isotopic composition of the mantle. Geochim. Cosmochim. Acta *199*, 196–209.

Gaudin, A., Grauby, O., Noack, Y., Decarreau, A., and Petit, S. (2004). Accurate crystal chemistry of ferric smectites from the lateritic nickel ore of Murrin Murrin (Western Australia). I. XRD and multi-scale chemical approaches. Clay Miner. *39*, 301–315.

Gaudin, A., Decarreau, A., Noack, Y., and Grauby, O. (2005). Clay mineralogy of the nickel laterite ore developed from serpentinised peridotites at Murrin Murrin, Western Australia. Aust. J. Earth Sci. *52*, 231–241.

Gleeson, S.A., Butt, C.R.M., and Elias, M. (2003). Nickel laterite: a review. Society of Economic Geologists Newsletter 1,12-18.

Gleeson, S.A., Herrington, R.J., Durango, J., Velásquez, C.A., and Koll, G. (2004). The mineralogy and geochemistry of the Cerro Matoso SA Ni laterite deposit, Montelíbano, Colombia. Econ. Geol. *99*, 1197–1213.

Golightly, J.P. (1981). Nickeliferous laterite deposits. Econ. Geol. *75th anniversary Volume*, 710–735.

Golightly, J.P. (2010). Progress in understanding the evolution of nickel laterites. Chall. Find. New Miner. Resour. Glob. Metallog. Innov. Explor. New Discov. *2*, 451–475.

Gramlich, J.W., Machlan, L., Barnes, I.L., and Paulsen, P.J. (1989). Absolute isotopic abundance ratios and atomic weight of a reference sample of nickel. J. Res. Natl. Inst. Stand. Technol. *94*, 347–356.

Gueguen, B., Rouxel, O., Ponzevera, E., Bekker, A., and Fouquet, Y. (2013). Nickel Isotope Variations in Terrestrial Silicate Rocks and Geological Reference Materials Measured by MC-ICP-MS. Geostand. Geoanalytical Res. *37*, 297–317.

Gueguen, B., Rouxel, O., Rouget, M.-L., Bollinger, C., Ponzevera, E., Germain, Y., and Fouquet, Y. (2016). Comparative geochemistry of four ferromanganese crusts from the Pacific Ocean and significance for the use of Ni isotopes as paleoceanographic tracers. Geochim. Cosmochim. Acta *189*, 214–235.

Guillot, S., and Hattori, K. (2013). Serpentinites: essential roles in geodynamics, arc volcanism, sustainable development, and the origin of life. Elements *9*, 95–98.

Hofmann, A., Bekker, A., Dirks, P., Gueguen, B., Rumble, D., and Rouxel, O.J. (2014). Comparing orthomagmatic and hydrothermal mineralization models for komatiite-hosted nickel deposits in Zimbabwe using multiple-sulfur, iron, and nickel isotope data. Miner. Deposita *49*, 75–100.

Kiczka, M., Wiederhold, J.G., Frommer, J., Voegelin, A., Kraemer, S.M., Bourdon, B., and Kretzschmar, R. (2011). Iron speciation and isotope fractionation during silicate weathering and soil formation in an alpine glacier forefield chronosequence. Geochim. Cosmochim. Acta *75*, 5559–5573.

Montarges-Pelletier, E., Chardot, V., Echevarria, G., Michot, L.J., Bauer, A., and Morel, J.-L. (2008). Identification of nickel chelators in three hyperaccumulating plants: an X-ray spectroscopic study. Phytochemistry *69*, 1695–1709.

Moynier, F., Blichert-Toft, J., Telouk, P., Luck, J.-M., and Albarède, F. (2007). Comparative stable isotope geochemistry of Ni, Cu, Zn, and Fe in chondrites and iron meteorites. Geochim. Cosmochim. Acta *71*, 4365–4379.

Porter, S.J., Selby, D., and Cameron, V. (2014). Characterising the nickel isotopic composition of organic-rich marine sediments. Chem. Geol. *387*, 12–21.

Quitte, G., and Oberli, F. (2006). Quantitative extraction and high precision isotope measurements of nickel by MC-ICPMS. J. Anal. At. Spectrom. *21*, 1249–1255.

Raous, S., Echevarria, G., Sterckeman, T., Hanna, K., Thomas, F., Martins, E.S., and Becquer, T. (2013). Potentially toxic metals in ultramafic mining materials: identification of the main bearing and reactive phases. Geoderma *192*, 111–119.

Ratié, G., Jouvin, D., Garnier, J., Rouxel, O., Miska, S., Guimarães, E., Cruz Vieira, L., Sivry, Y., Zelano, I., Montarges-Pelletier, E., et al. (2015). Nickel isotope fractionation during tropical weathering of ultramafic rocks. Chem. Geol. *402*, 68–76.

Ratié, G., Quantin, C., Jouvin, D., Calmels, D., Ettler, V., Sivry, Y., Vieira, L.C., Ponzevera, E., and Garnier, J. (2016). Nickel isotope fractionation during laterite Ni ore smelting and refining: Implications for tracing the sources of Ni in smelter-affected soils. Appl. Geochem. *64*, 136–145.

Ravel, B., and Newville, M. (2005). ATHENA, ARTEMIS, HEPHAESTUS: data analysis for X-ray absorption spectroscopy using IFEFFIT. J. Synchrotron Radiat. *12*, 537–541.

Roqué-Rosell, J., Villanova-de-Benavent, C., and Proenza, J.A. (2016). The accumulation of Ni in serpentines and garnierites from the Falcondo Ni-laterite deposit (Dominican Republic) elucidated by means of μXAS. Geochim. Cosmochim. Acta.

Schauble, E.A. (2004). Applying stable isotope fractionation theory to new systems. Rev. Mineral. Geochem. *55*, 65–111.

Siebert, C., Nagler, T.F., and Kramers, J.D. (2001). Determination of molybdenum isotope fractionation by double-spike multicollector inductively coupled plasma mass spectrometry. Geochem. Geophys. Geosystems *2*, art. no.-2000GC000124.

Tirez, K., Silversmit, G., Vincze, L., Servaes, K., Vanhoof, C., Mertens, M., Bleux, N., and Berghmans, P. (2011). Speciation and fractionation of nickel in airborne particulate matter: comparison between selective leaching and XAS spectroscopy. J. Anal. At. Spectrom. *26*, 517–527.

Trescases, J.J. (1975). L'évolution géochimique supergène des roches ultrabasiques en zone tropicale - Formation des gisements nickélifères de Nouvelle-Calédonie. Mémoire O.R.S.T.O.M., n°78, 259 p.

Trescases, J.-J. (1979). Remplacement progressif des silicates par les hydroxides de fer et de nickel dans les profils d'altération tropicale des roches ultrabasiques. Accumulation résiduelle et épigénie. Sci Geol Bull *32*, 181–188.

Trescases, J.-J., Melfi, A.J., and de Oliveira, S.B. (1981). Nickeliferous laterites of Brazil. In: Laterization processes. IBH Publishing. New Delhi, pp 170-184.

Vance, D., Little, S.H., Archer, C., Cameron, V., Andersen, M.B., Rijkenberg, M.J.A., and Lyons, T.W. (2016). The oceanic budgets of nickel and zinc isotopes: the importance of sulfidic environments as illustrated by the Black Sea. Philos. Trans. R. Soc. Math. Phys. Eng. Sci. *374*.

Vance, D., Archer, C., Little, S.H., Köbberich, M., and de Souza, G.F. (2017). The oceanic cycles of the transition metals and their isotopes. Acta Geochim. 1–4.

Vasconcelos, P.M., Reich, M., and Shuster, D.L. (2015). The paleoclimatic signatures of supergene metal deposits. Elements *11*, 317–322.

Villanova-de-Benavent, C., Domènech, C., Tauler, E., Galí, S., Tassara, S., and Proenza, J.A. (2016). Fe–Ni-bearing serpentines from the saprolite horizon of Caribbean Ni-laterite deposits: new insights from thermodynamic calculations. Miner. Deposita 1–14.

Wang, S.-J., and Wasylenki, L.E. (2017). Experimental constraints on reconstruction of Archean seawater Ni isotopic composition from banded iron formations. Geochim. Cosmochim. Acta *206*, 137–150.

Wasylenki, L.E., Howe, H.D., Spivak-Birndorf, L.J., and Bish, D.L. (2015). Ni isotope fractionation during sorption to ferrihydrite: Implications for Ni in banded iron formations. Chem. Geol. *400*, 56–64.

Wells, M.A., Ramanaidou, E.R., Verrall, M., and Tessarolo, C. (2009). Mineralogy and crystal chemistry of "garnierites" in the Goro lateritic nickel deposit, New Caledonia. Eur. J. Mineral. *21*, 467–483.

Wiederhold, J.G., Kraemer, S.M., Teutsch, N., Borer, P.M., Halliday, A.N., and Kretzschmar, R. (2006). Iron isotope fractionation during proton-promoted, ligand-controlled, and reductive dissolution of goethite. Environ. Sci. Technol. *40*, 3787–3793.

Wiederhold, J.G. (2015). Metal Stable Isotope Signatures as Tracers in Environmental Geochemistry. Environ. Sci. Technol. *49*, 2606–2624.

Figure captions

Figure 1: Sketch map of studied area (RC and BA weathering profiles, PZ1 and PZ2 piezometers). Serra da Malacheta: metabasalt, metagranitoide and gneiss, TQDL: Tiertiary and Quarternary Sediments, Ultramafic zone: serpentinite, dunite, harzburgite and pyroxene, Mafic Zone: anorthosite, norite and gabbro. Geological sources: CPRM GOIAS.

Figure 2: Vertical changes in the bulk content of Fe, Mg, Si, Mn, Ni and Cr, the mineralogy and the Ni isotope values (δ^{60}Ni in ‰) in RC (a) and BA (b) lateritic profiles. Black lines indicate the different units of the profile: L: Laterite, S: Saprolite, SM: SMectitic horizon, SR: SapRock. The δ^{60}Ni value of the parent composition (deepest sample) is represented by a grey rectangle along the profile. Arrows indicate samples analyzed by XAS.

Figure 3: Transmission electron microscopy images showing minerals typically found in the lateritic unit (a, b, RC 4-5), the top of saprolitic unit (c, d, RC 16-17) and the bottom part of saprolitic unit (e, f, RC 20-21). Ni content is expressed in mass %. Symbols for mineral species: G for goethite, Sp for serpentine, Sm for smectite.

Figure 4: Normalized XANES at the Ni K-edge of the spectra for a) references and b) selected RC samples (n=14).

Figure 5: Results of the LC-LSF fits of experimental XANES spectra for RC selected sample (n=14). The accuracy of this LC-LSF procedure is considered to be ±10%.

Figure 6: Nickel isotope data (δ^{60}Ni in ‰) plotted against Mg/Ni molar ratio for both profiles (RC & BA), serpentinite, lateritic samples (Ratié et al., 2015) and UM soils from Barro Alto (Ratié et al., 2015, 2016). δ^{60}Ni mean value was calculated for laterite units including chalcedony intrusion (Avg laterite BA and RC). The 2 SD error shown for δ^{60}Ni values on the figure is based on replicate measurements by MC-ICP-MS, except for Avg laterite BA and RC, where SD is calculated on all laterite samples for RC (n=14) and BA (n=15) profiles. Bulk Silicate Earth values from Gueguen et al. (2013) and Gall et al. (2017) are represented.

Figure 7: % of Ni associated to goethite (a) and 2:1 phyllosilicates (b) and the Ni isotope composition (δ^{60}Ni in ‰) of samples analyzed by XAS (n=14). The samples are representative of the three sections identified, i.e. laterite, saprolite, saprock. Error bars are 2 SD for Ni isotope measurement and ±10% for the Ni proportion associated to goethite and 2:1 phyllosilicates.

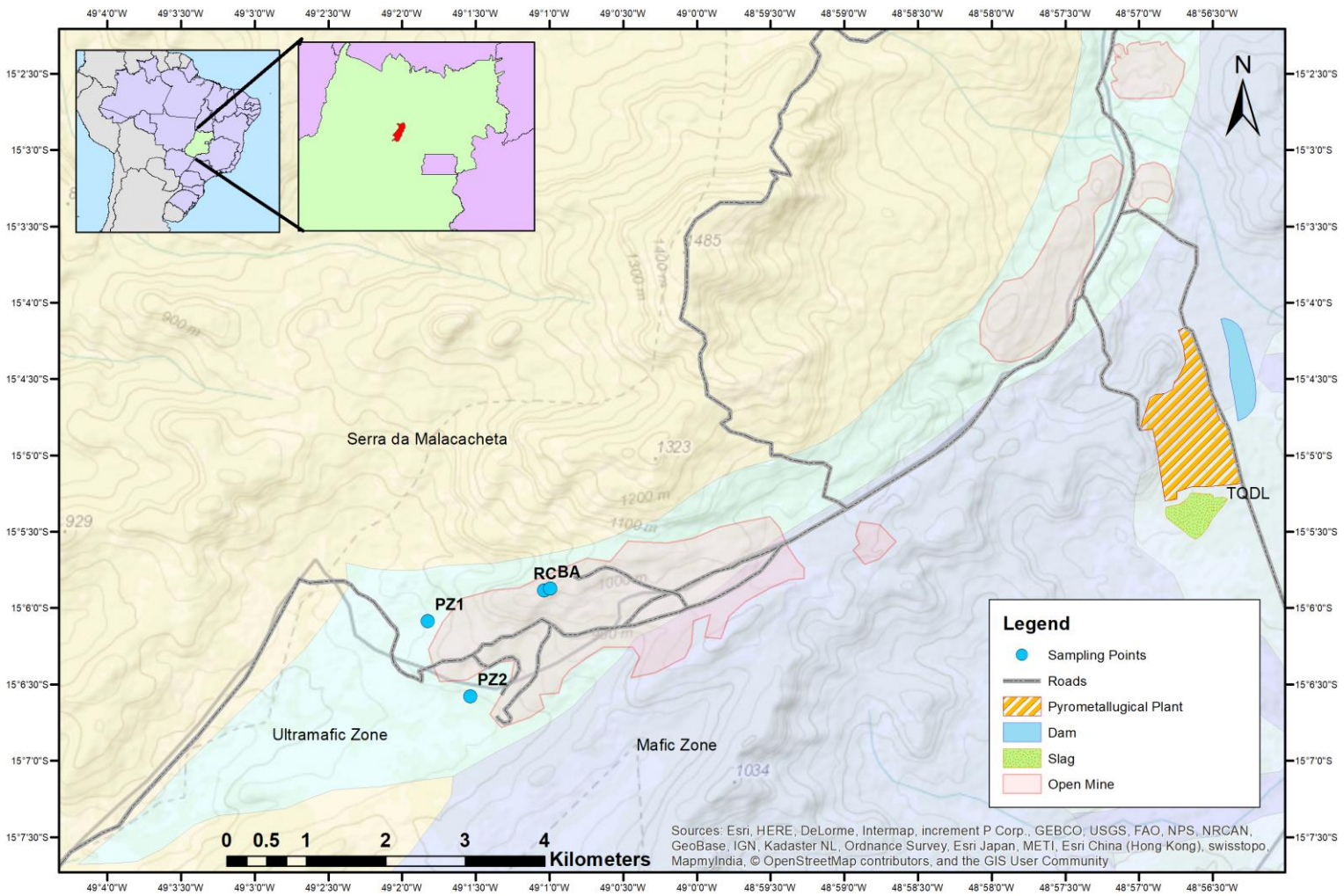

Figure 1

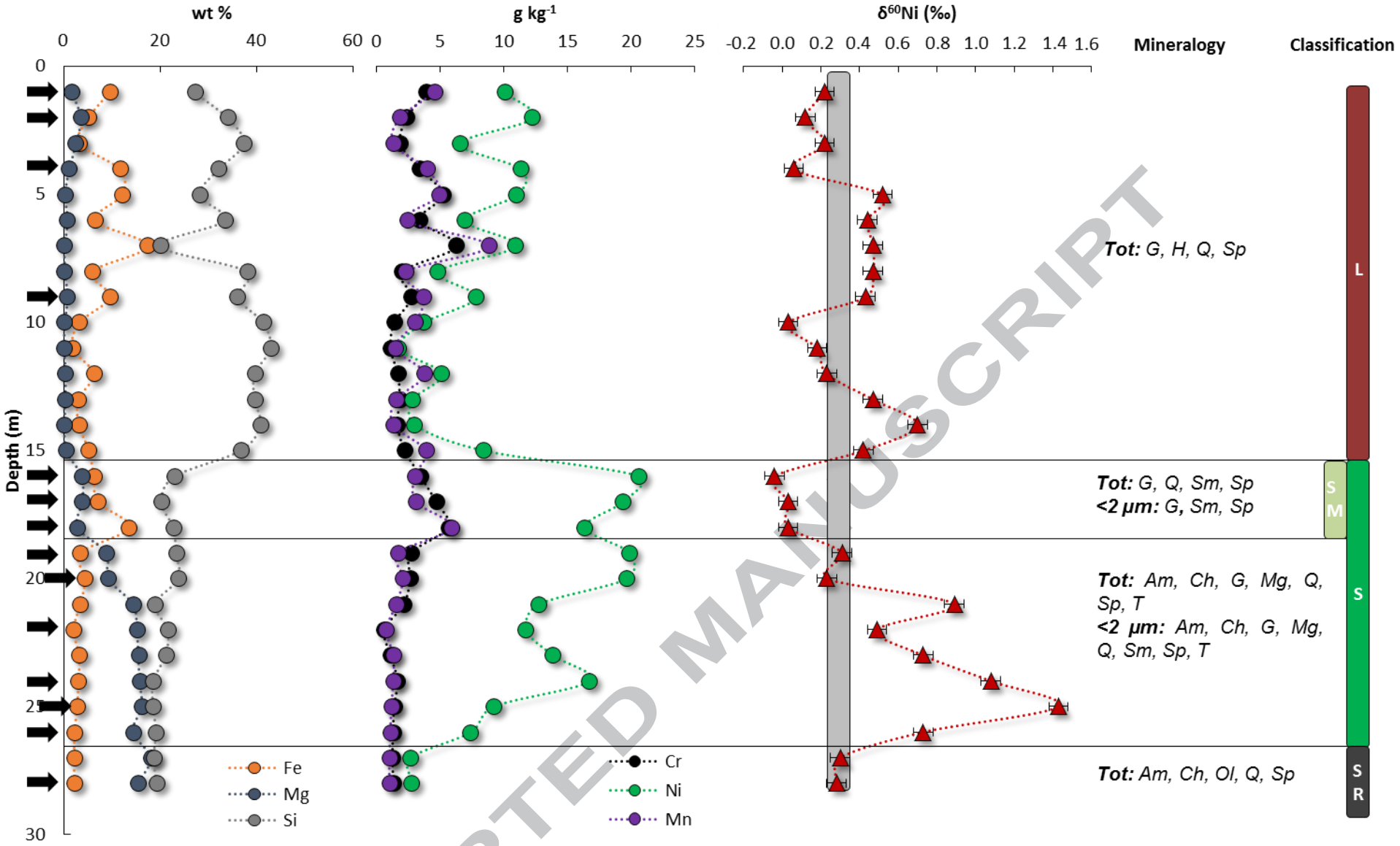

Figure 2a

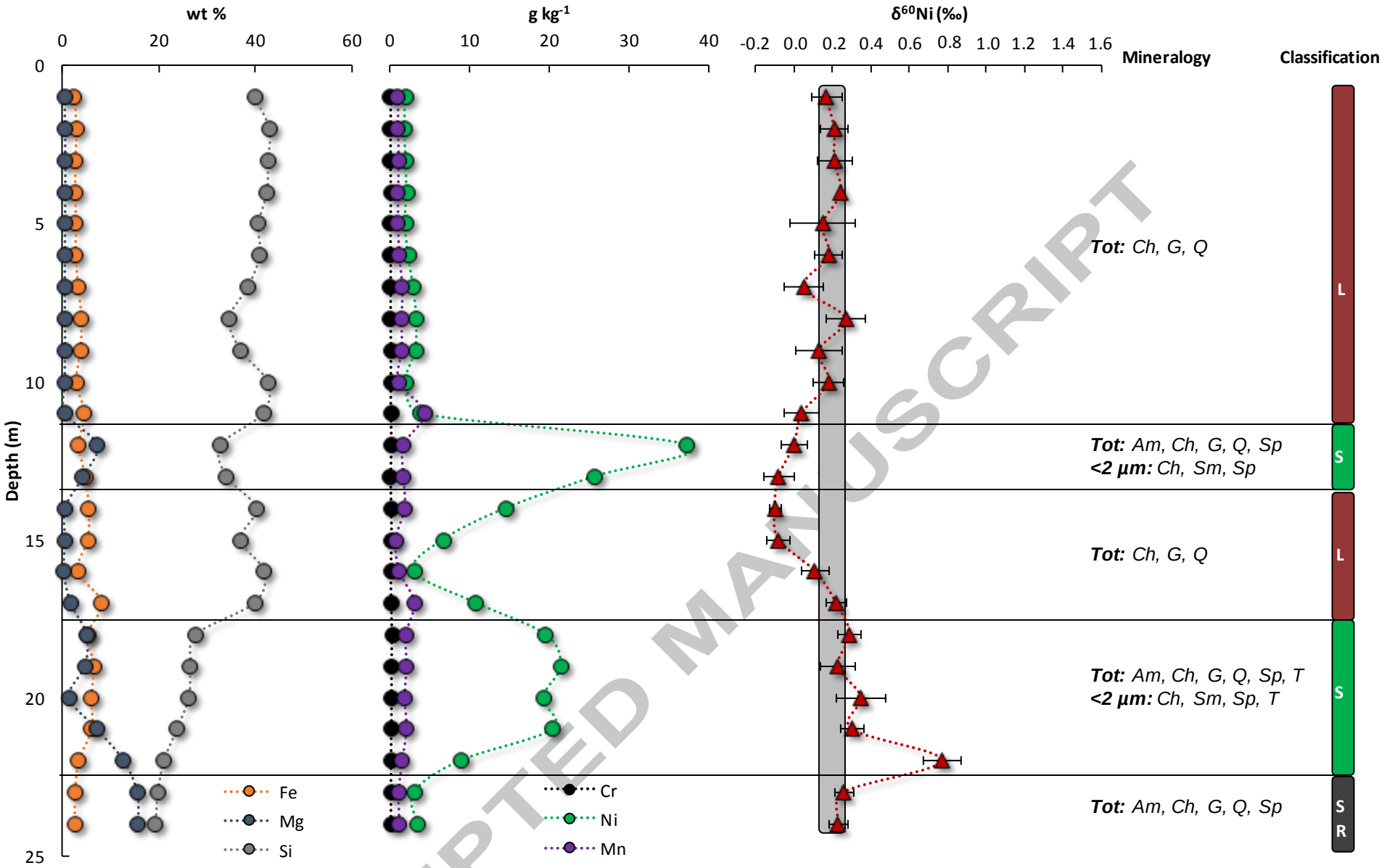

Figure 2b

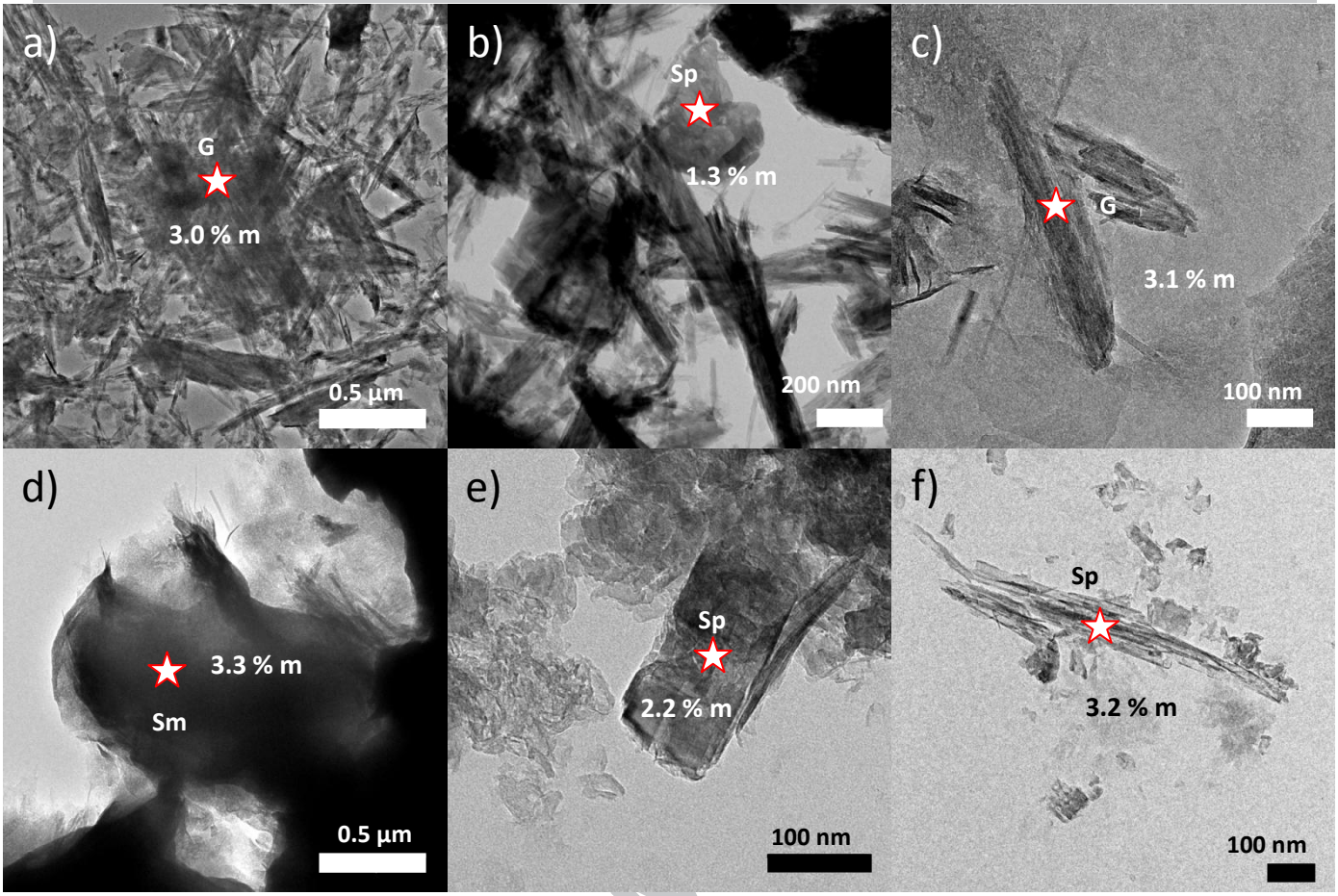

Figure 3

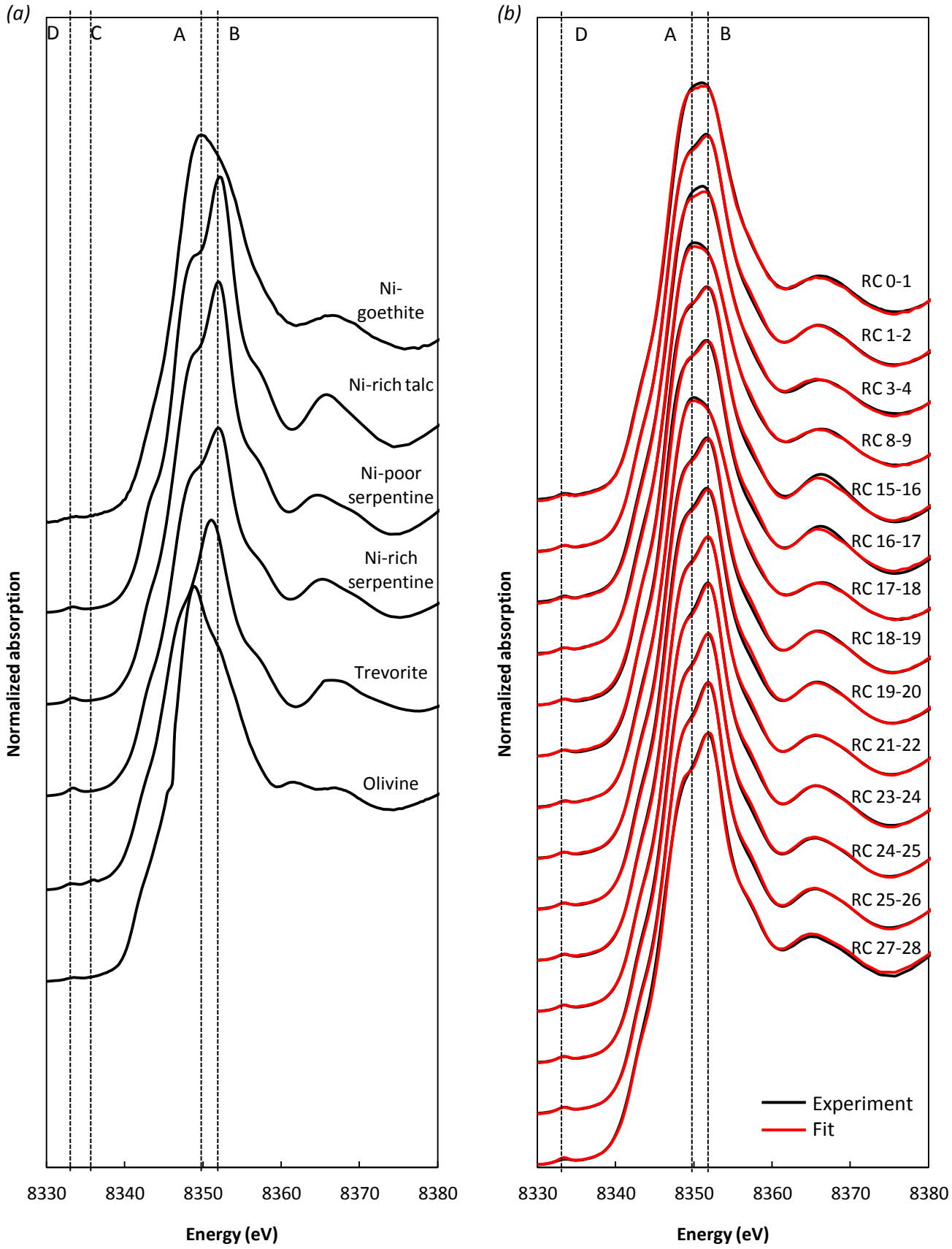

Figure 4

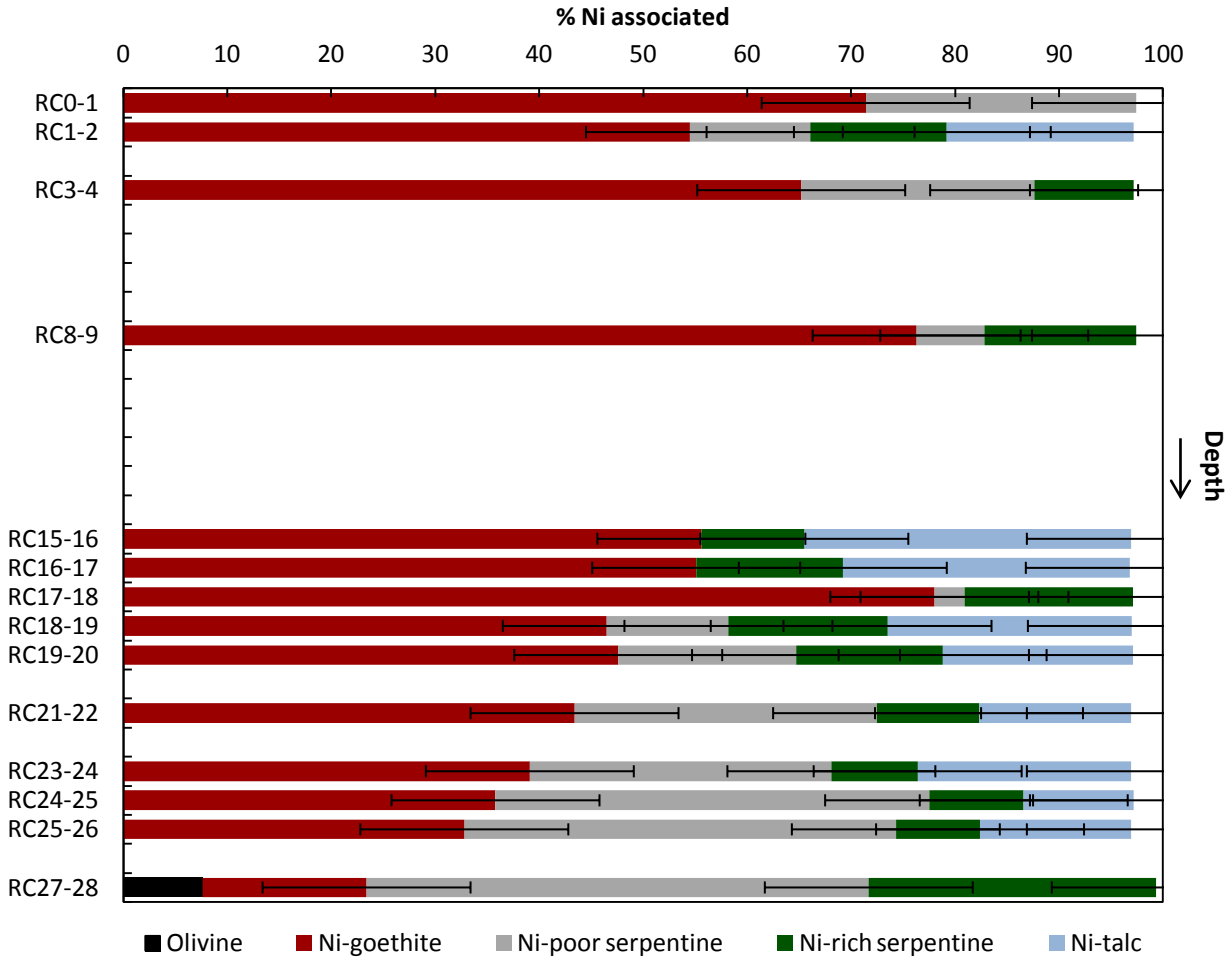

Figure 5

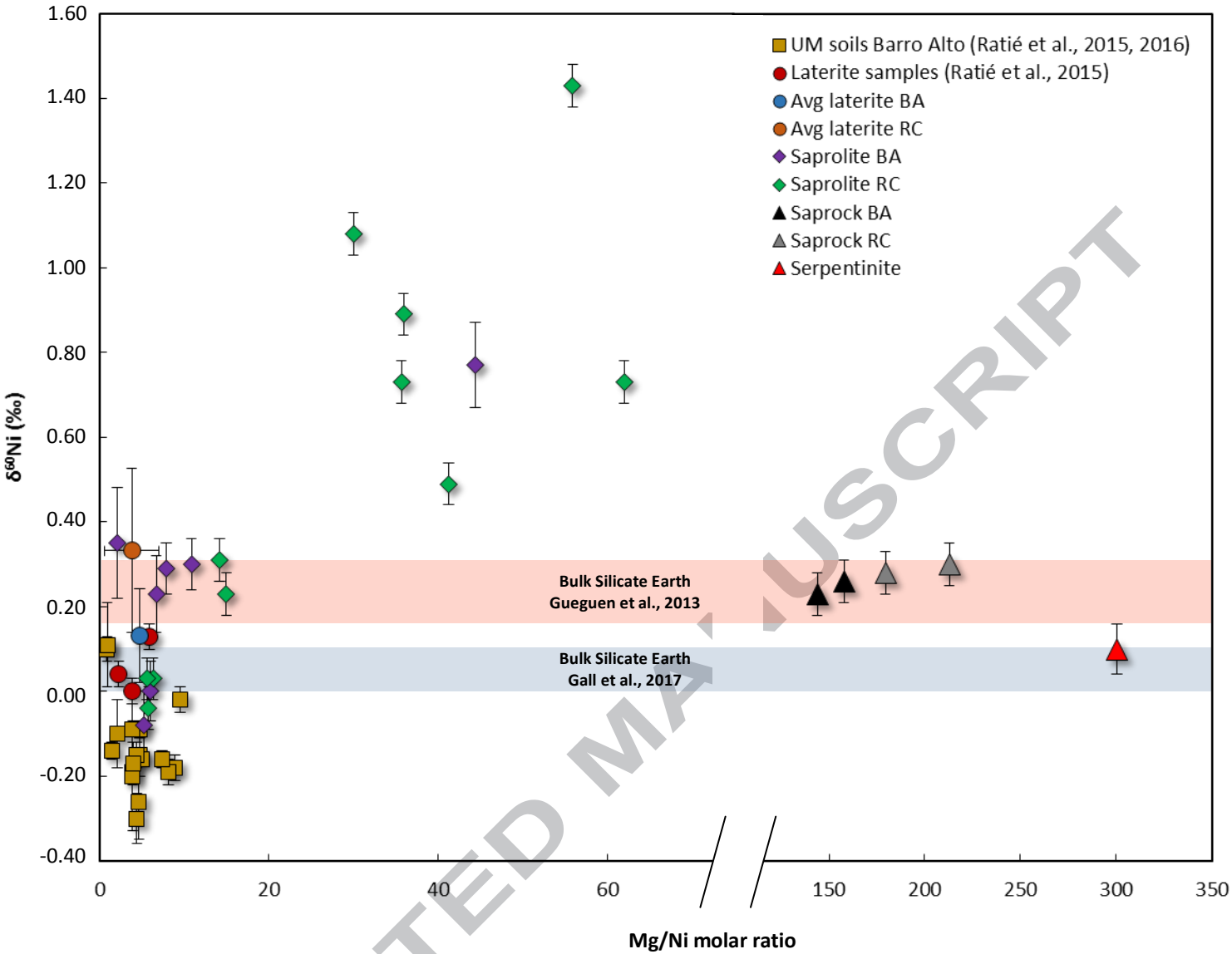

Figure 6

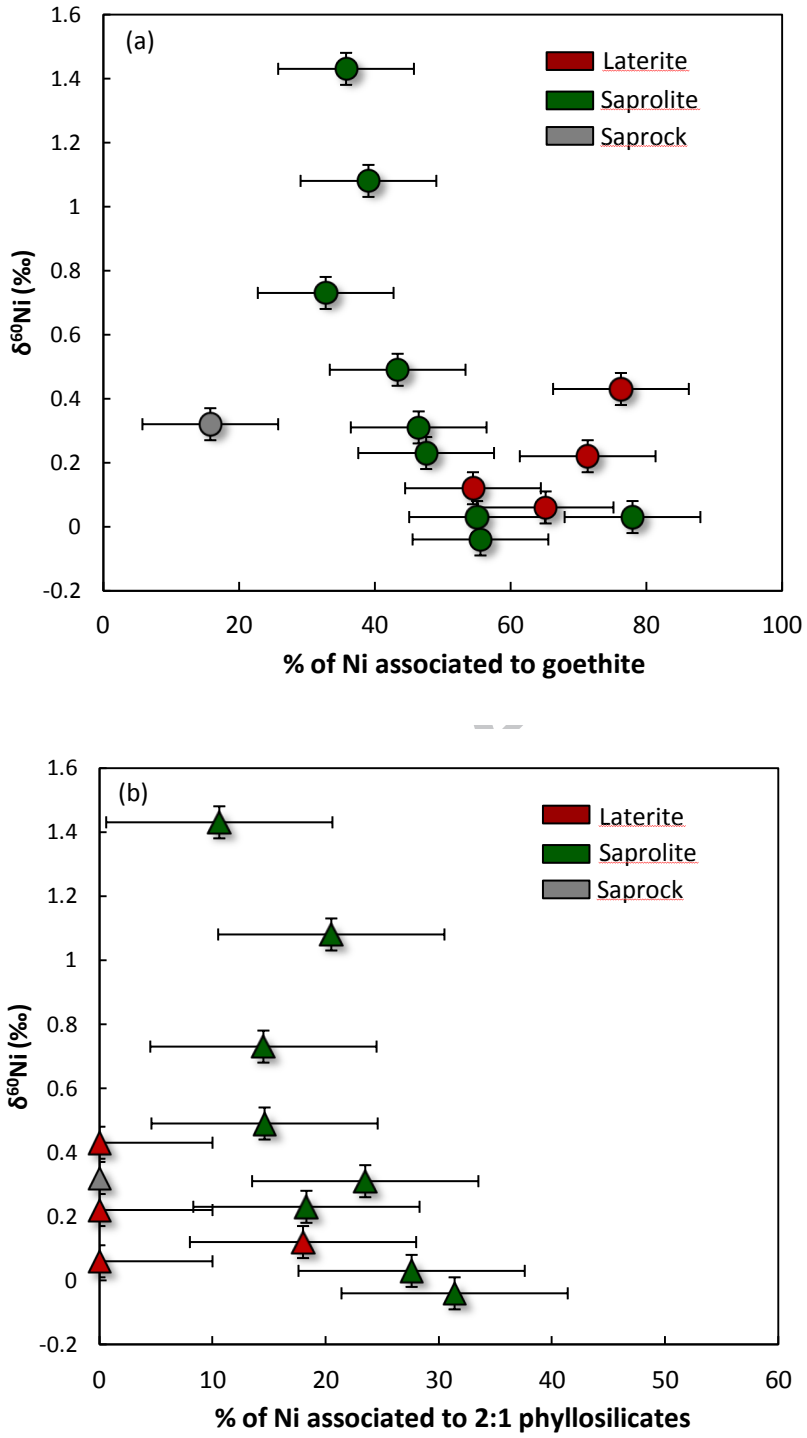

Figure 7

Table captions

Table 1: Chemical and mineralogical characteristics of RC profile. Cobalt and Ti contents have been measured by ICP-OES. All other element contents have been measured by AAS (q.l. refers to the quantification limit; n.d.: not determined). Ni isotope composition (δ^{60}Ni) is expressed in ‰ and 2 SD values are calculated from replicate measurements. Sm: Smectite, Sp: Serpentine, Ch: Chlorite, T: Talc, H: Hematite, Mg: Magnetite, G: Goethite, Q: Quartz, Am: Amphibole, Ol: Olivine (+++ abundant, ++ common, + minor, (+) traces). XRD on clay fraction (< 2 µm) was only performed on saprolitic samples.

Table 2: Chemical and mineralogical characteristics of BA profile. Cobalt and Ti contents have been measured by ICP-OES. All other element contents have been measured by AAS (q.l. refers to the quantification limit; n.d.: not determined). Ni isotope composition (δ^{60}Ni) is expressed in ‰ and 2 SD values are calculated from replicate measurements. Sm: Smectite, Sp: Serpentine, Ch: Chlorite, T: Talc, G: Goethite, Q: Quartz, Am: Amphibole (+++ abundant, ++ common, + minor, (+) traces). XRD on clay fraction (< 2 µm) was only performed on saprolitic samples.

Table 3: Cation Exchange Capacity (CEC) with the proportion of exchangeable Ni in the RC profile samples $[Ni]_{CEC}$ *and the* $\delta^{60}Ni$ *values for the extracted solution (*$\delta^{60}Ni_{CEC\text{-}solution}$*) and the residue (*$\delta^{60}Ni_{CEC\text{-}residue}$*), *n=2. (n.d.: not determined).*

Calculated bulk composition ($\delta^{60}Ni_{total\text{-}calculated}$*) based on the sum of the exchangeable extract and the residue and their respective pool sizes:* $\delta^{60}Ni_{total\text{-}recalculated}$*: A;* $\delta^{60}Ni_{CEC\text{-}solution}$*: B;* $\delta^{60}Ni_{CEC\text{-}residue}$*: C;* $[Ni]_{total}$ *: X ;* $[Ni]_{CEC\text{-}solution}$ *: Y ;* $[Ni]_{CEC\text{-}residue}$ *: Z.*

$A*X = B*Y + C*Z \leftrightarrow A = (B*Y + C*Z) / X$; *the error bars of the* $\delta^{60}Ni_{total\text{-}recalculated}$ *are calculated with the following equation:* $2SD_{total\text{-}recalculated} = \sqrt{(2SD_{CEC\text{-}solution})^2+(2SD_{CEC\text{-}residue})^2}$

Table 4: Element concentration after filtration (<0.45µm, q.l. refers to the quantification limit) and Ni isotopic composition (δ^{60}Ni in ‰) of the groundwater samples collected in the Barro Alto massif, during the dry season (2014) and the rainy season (2015).

Sample name	depth (m)	Fe	Mg	Si	Al	Cr	Mn	Ni	Ca	Co	K	Na	Ti	$\delta^{60/58}$Ni	2 S.D.	XRD Bulk										XRD clay fraction							
		%			g kg^{-1}				mg kg^{-1}					(‰)		Sm	Sp	Ch	T	H	Mg	G	Q	Am	Ol	Sm	Sp	Ch	T	Mg	G	Q
RC0-1	0-1	9.65	1.81	27.3	3.97	3.93	4.57	10.1	364	602	63	< q.l.	249	0.22	0.05	(+)	++	+++		(+)		+	++										
RC1-2	1-2	5.18	3.62	34.2	0.79	2.36	1.86	12.3	307	260	86	< q.l.	46	0.12	0.05		++			+		+	+++										
RC2-3	2-3	3.36	2.59	37.5	0.53	1.88	1.32	6.52	247	156	79	< q.l.	26	0.22	0.05		++					+	+										
RC3-4	3-4	11.7	1.21	32.3	11.6	3.42	3.95	11.3	44	729	29	< q.l.	281	0.06	0.05		++	(+)				+	+++										
RC4-5	4-5	12.2	0.30	28.3	1.85	5.20	4.96	11.0	41	552	24	< q.l.	147	0.52	0.05					+		+	+										
RC5-6	5-6	6.61	0.84	33.5	0.79	3.39	2.40	6.92	42	267	23	< q.l.	40	0.44	0.05		+					+	+										
RC6-7	6-7	17.5	0.24	20.2	7.41	6.29	8.83	10.9	45	855	16	< q.l.	490	0.47	0.05							++	++										
RC7-8	7-8	6.05	0.24	38.2	1.06	2.02	2.32	4.79	49	237	28	< q.l.	70	0.47	0.05					+		+	++										
RC8-9	8-9	9.65	0.84	36.2	1.85	2.74	3.72	7.78	119	444	29	< q.l.	110	0.43	0.05							+	+++										
RC9-10	9-10	3.29	0.24	41.6	0.26	1.40	3.02	3.69	40	278	51	< q.l.	20	0.03	0.05					+		+	++										
RC10-11	10-11	1.99	0.12	43.1	< q.l.	1.09	1.47	1.73	42	170	42	< q.l.	7	0.18	0.05					+		+	+++										
RC11-12	11-12	6.29	0.42	39.8	0.79	1.68	3.80	5.11	67	398	87	< q.l.	44	0.23	0.05					+		+	++										
RC12-13	12-13	3.11	0.30	39.8	0.26	1.81	1.55	2.83	53	158	43	< q.l.	15	0.47	0.05					+		+	++										
RC13-14	13-14	3.18	0.24	41.0	< q.l.	1.64	1.32	2.99	39	153	36	< q.l.	11	0.70	0.05					+		+	++										
RC14-15	14-15	5.32	0.48	36.9	1.32	2.22	3.87	8.41	51	493	24	< q.l.	360	0.42	0.05	(+)				+		+	++										
RC15-16	15-16	6.29	3.80	23.2	4.23	3.46	3.02	20.6	130	643	20	< q.l.	282	-0.04	0.05	++	+				+	+	+			+++	+	(+)			(+)		
RC16-17	16-17	7.17	3.92	20.4	4.76	4.69	3.10	19.3	94	544	61	< q.l.	288	0.03	0.05	+++	+	++				+	+			+++	++	(+)			+		
RC17-18	17-18	13.7	2.89	22.9	0.79	5.64	5.89	16.3	66	976	10	< q.l.	65	0.03	0.05		+					++	+							+++			
RC18-19	18-19	3.50	8.99	23.5	0.53	2.70	1.70	19.9	89	220	24	< q.l.	48	0.31	0.05		+++		+		+	+	+			+	++	(+)	(+)		+	+	
RC19-20	19-20	4.51	9.35	23.9	0.79	2.63	2.09	19.6	122	265	18	< q.l.	35	0.23	0.05		+++		++		+	+	+			+	++	(+)	+		+	+	
RC20-21	20-21	3.53	14.53	19.1	0.79	2.16	1.55	12.7	595	138	5	< q.l.	40	0.89	0.05		+++					+	(+)			(+)	+++	(+)			+	(+)	
RC21-22	21-22	2.06	15.38	21.7	< q.l.	0.62	0.77	11.7	91	112	12	< q.l.	11	0.49	0.05		+++				+	+	+				+++			+	+	+	
RC22-23	22-23	3.29	15.68	21.3	0.26	1.09	1.32	13.8	251	146	12	< q.l.	25	0.73	0.05		+++				+	+	+			(+)	+++				+	+	
RC23-24	23-24	3.11	15.92	18.7	0.79	1.64	1.32	16.7	2031	114	38	116.8	93	1.08	0.05		+++	++			+	(+)		+		(+)	+++	(+)			(+)	(+)	
RC24-25	24-25	2.87	16.40	18.7	1.85	1.37	1.16	9.19	1908	98	18	104.6	116	1.43	0.05		+++					(+)	(+)	+		(+)	+++	(+)		+	(+)	(+)	
RC25-26	25-26	2.31	14.53	19.3	1.59	1.30	1.08	7.39	1235	99	13	50.07	95	0.73	0.05		+++	++					(+)			(+)		+	+	+	(+)	(+)	
RC26-27	26-27	2.24	18.27	18.8	1.59	1.23	1.01	2.67	2467	87	19	114.2	101	0.30	0.05		+++	+					(+)	+	+		+++			+		(+)	
RC27-28	27-28	2.24	15.62	19.4	0.79	1.33	1.01	2.75	98	103	8	< ql	207	0.28	0.05		+++	++					(+)		+		+++	+		+		(+)	
Serpentinite		3.04	24.06	n.d.	0.26	n.d.	1.63	2.51	1655	n.d.	20	57.86	n.d.	0.10	0.06		+++																

Table 1

Sample name	depth (m)	Fe	Mg	Si	Al	Cr	Mn	Ni	Ca	Co	K	Na	Ti	$\delta^{60/58}$Ni	2 S.D.	XRD Bulk							XRD clay fraction					
		%			g kg^{-1}				mg kg^{-1}					(‰)		Sm	Sp	Ch	T	G	Q	Am	Sm	Sp	Ch	T	G	Q
BA0-1	0-1	2.41	0.36	40.0	< q.l.	0.10	1.01	1.96	134	115	22	< q.l.	22	0.17	0.08			(+)		(+)	+++								
BA1-2	1-2	2.80	0.42	43.0	< q.l.	0.10	1.01	1.89	52	116	21	< q.l.	15	0.21	0.07			(+)		(+)	+++								
BA2-3	2-3	2.59	0.48	42.7	< q.l.	0.07	1.08	2.04	47	115	21	< q.l.	24	0.21	0.09			(+)		(+)	+++								
BA3-4	3-4	2.55	0.48	42.4	< q.l.	0.14	1.01	2.12	43	117	20	< q.l.	59	0.24	0.01			(+)		(+)	+++								
BA4-5	4-5	2.69	0.42	40.7	< q.l.	0.07	1.01	1.96	44	112	20	< q.l.	48	0.15	0.17					(+)	+++								
BA5-6	5-6	2.66	0.42	41.0	< q.l.	0.10	1.16	2.36	70	126	23	< q.l.	17	0.18	0.07					(+)	+++								
BA6-7	6-7	3.18	0.36	38.4	0.53	0.10	1.55	2.99	53	271	41	< q.l.	30	0.05	0.10					(+)	+++								
BA7-8	7-8	3.85	0.42	34.5	0.26	0.10	1.47	3.38	135	200	28	< q.l.	35	0.27	0.10			(+)		(+)	+++								
BA8-9	8-9	3.67	0.42	36.9	0.26	0.14	1.47	3.22	96	209	28	< q.l.	27	0.13	0.12			(+)		(+)	+++								
BA9-10	9-10	2.76	0.36	42.5	< q.l.	0.14	1.08	2.04	81	72	27	< q.l.	16	0.18	0.08					(+)	+++								
BA10-11	10-11	4.44	0.48	41.7	1.59	0.14	4.41	3.93	3	693	22	< q.l.	332	0.04	0.09			+		(+)	+++								
BA11-12	11-12	3.36	7.12	32.8	12.4	0.24	1.70	37.4	3271	841	28	76	1357	0.00	0.07		(+)	+++		(+)	+	+	++	+	+++		+	++
BA12-13	12-13	4.62	4.22	34.0	2.65	0.10	1.70	25.6	355	849	27	< q.l.	239	-0.08	0.08		(+)	+++		(+)	+++	(+)	+		+		+	+++
BA13-14	13-14	5.39	0.42	40.2	0.26	0.21	1.86	14.5	60	1299	28	< q.l.	35	-0.10	0.03			(+)		(+)	+++								
BA14-15	14-15	5.18	0.42	36.9	0.79	0.27	0.70	6.68	275	507	24	< q.l.	80	-0.08	0.06			+		(+)	+++	+							
BA15-16	15-16	3.08	0.18	41.8	< q.l.	0.14	1.16	3.06	77	200	24	< q.l.	20	0.11	0.07			(+)		(+)	+++								
BA16-17	16-17	8.08	1.57	39.9	3.70	0.21	3.10	10.8	74	521	27	< q.l.	344	0.22	0.05			++	+	(+)	+++		(+)	+	+	+	++	+++
BA17-18	17-18	5.18	4.89	27.7	11.4	0.34	2.01	19.6	805	402	39	48	1858	0.29	0.06			+++		(+)	+	(+)	++	++	+++		(+)	+
BA18-19	18-19	6.43	4.58	26.5	8.20	0.27	2.09	21.5	2189	324	34	80	1144	0.23	0.09			+++		(+)	+	+	+++	++	++		++	+++
BA19-20	19-20	5.91	1.27	26.1	11.1	0.27	1.86	19.3	1159	298	38	72	2355	0.35	0.13			+++		(+)	+	(+)	++	++	+++		++	+
BA20-21	20-21	6.01	7.06	23.7	7.67	0.24	2.09	20.4	2227	311	34	101	1412	0.30	0.06		+	+++		(+)	+	+	++	++	+++		+	(+)
BA21-22	21-22	3.36	12.6	20.9	5.29	0.17	1.55	8.88	878	135	26	41	407	0.77	0.10	(+)	++	+++		(+)	+	+	+++	+++	++			(+)
BA22-23	22-23	2.52	15.4	19.7	1.06	0.17	1.08	3.06	2714	94	17	160	207	0.26	0.05		+++	++		(+)	(+)	++	+	+++	+			(+)
BA23-24	23-24	2.48	15.7	19.2	2.12	0.14	1.16	3.46	1978	100	16	113	144	0.23	0.05		+++	++		(+)	(+)	++	+	+++	+			(+)

Table 2

Sample name	depth (m)	$[Ni]_{total}$ mg kg^{-1}	$\delta^{60}Ni_{total}$ ‰	2 S.D	CEC $cmol_c$ kg^{-1}	$[Ni]_{CEC}$ mg kg^{-1}	$\delta^{60}Ni_{CEC\text{-}solution}$ ‰	$\delta^{60}Ni_{CEC\text{-}residue}$ ‰	$\delta^{60}Ni_{total\text{-}recalculated}$ ‰
RC0-1	0-1	10058	0.22	0.05	4.5	0.8	n.d.	n.d.	n.d.
RC3-4	3-4	11316	0.06	0.05	3	22.9	n.d.	n.d.	n.d.
RC4-5	4-5	11001	0.52	0.05	2.2	4	n.d.	n.d.	n.d.
RC6-7	6-7	10923	0.47	0.05	3.7	12.4	n.d.	n.d.	n.d.
RC11-12	11-12	5108	0.23	0.05	0.8	2.6	n.d.	n.d.	n.d.
RC13-14	13-14	2986	0.7	0.05	0.7	0.8	n.d.	n.d.	n.d.
RC15-16	15-16	20588	-0.04	0.05	55.3	1454	0.28 ± 0.06	-0.13 ± 0.07	-0.10 ± 0.09
RC16-17	16-17	19331	0.03	0.05	59.3	1733	0.26* ± 0.16	-0.03 ± 0.06	0.00 ± 0.17
RC17-18	17-18	16345	0.03	0.05	7.8	157	0.31 ± 0.05	-0.04 ± 0.06	-0.04 ± 0.08
RC19-20	19-20	19645	0.23	0.05	11.8	98.5	0.96 ± 0.05	0.28 ± 0.09	0.28 ± 0.10
RC21-22	21-22	11708	0.49	0.05	1.9	9.3	n.d.	n.d.	n.d.
RC23-24	23-24	16738	1.08	0.05	5.6	18.2	n.d.	n.d.	n.d.
RC24-25	24-25	9194	1.43	0.05	5.7	1.4	n.d.	n.d.	n.d.
RC25-26	25-26	7387	0.73	0.05	2.6	3.6	n.d.	n.d.	n.d.

Table 3

Sample name	pH	Ca	Mg	K	Si	Ni	$\delta^{60}Ni$	2 SD
		mg L^{-1}				µg L^{-1}	‰	
PZ1-2014	7.5	1.5	25.5	0.2	39.0	17.0	2.27	0.08
PZ2-2014	9.1	2.0	21.2	0.2	14.6	59.0	n.d.	n.d.
PZ1-2015	7.8	1.5	16.0	0.2	23.0	7.0	2.20	0.09
PZ2-2015	9.3	2.0	17.8	0.2	8.3	< q.l.	n.d.	n.d.

Table 4